# Turbulence characteristics over k-type rib roughened porous walls

# Turbulence characteristics over k-type rib roughened porous walls

Yuki Okazaki, Ayumi Shimizu, Yusuke Kuwata, Kazuhiko Suga*

*Department of Mechanical Engineering, Osaka Prefecture University, Sakai, Osaka 599–8531, Japan*

**Abstract**

To understand the permeability effects on turbulent rib-roughened porous channel flows, particle image velocimetry measurements are performed at the bulk Reynolds number of 5000 – 20000. Solid impermeable and porous ribs are considered for the rib-roughness whose geometry is categorised in the k-type roughness whose pitch/rib-height is 10. Three isotropic porous media with nearly the same porosity: 0.8, and different permeabilities (0.004, 0.020, 0.033 mm$^2$) are applied. It is observed that the recirculation between the ribs becomes weak and the recirculation vortex submerges into the porous wall as the wall permeability and Reynolds number increase for both solid and porous rib cases while the recirculation vanishes in high permeable cases. These phenomena result in the characteristic difference in the turbulence quantities. By fitting the mean velocity profiles to the log-law form, the permeability effects of both rib and bottom wall on the log-law parameters and the equivalent sand-grain roughness are discussed. It is concluded that the zero-plane displacement increases while the von Kármán constant and

*Corresponding author

*Email address:* `suga@me.osakafu-u.ac.jp` (Kazuhiko Suga)

the equivalent sand-grain roughness decrease as the wall and rib permeability increases.

*Keywords:* Porous walled channel, Rib-roughened wall, k-type roughness, PIV measurement

---

## List of Symbols

| | |
|---|---|
| $c_D$ | drag coefficient |
| $C^F$ | Forchheimer coefficient |
| $d_0$ | zero-plane displacement |
| $h$ | roughness scale |
| $H$ | clear channel height |
| $k$ | rod (rib) height |
| $k_s$ | equivalent sand grain roughness height |
| $K$ | permeability |
| Q$m$ | $(m = 1 - 4)$; quadrant of the Reynolds shear stress |
| $\mathrm{Re}_b$ | bulk Reynolds number: $U_b H/\nu$ |
| $\mathrm{Re}_\tau$ | friction Reynolds number of the rough surface: $u_\tau^R y_m/\nu$ |
| $u, v$ | velocity components in the $x, y$ directions |
| $u_\tau^R$ | friction velocity by the total drag |
| $u_*$ | friction velocity for log-law |
| $U_b$ | bulk mean velocity |
| $w$ | rib spacing |
| $x$ | streamwise coordinate |

| | |
|---|---|
| $X_F$ | front location of a separation bubble |
| $X_R$ | reattachment length |
| $y$ | vertical coordinate |
| $\hat{y}$ | wall coordinate |
| $y_0$ | zero shear stress location |
| $y_m$ | maximum mean velocity location |
| $z$ | spanwise coordinate |
| $\Delta U^+$ | roughness function |
| $\kappa$ | von Kármán constant |
| $\lambda$ | centre to centre rib interval |
| $\nu$ | kinematic viscosity |
| $\rho$ | fluid density |
| $\tau^R$ | total drag |
| $\tau_d$ | form drag |
| $\tau_w$ | viscous drag |
| $\varphi$ | porosity |
| $\overline{\phi}$ | Reynolds averaged value of $\phi$ |
| $\phi'$ | fluctuation of $\phi$: $\phi - \overline{\phi}$ |
| $[\phi]$ | superficial plane-averaged value of $\phi$ |
| $[\phi]^f$ | fluid phase plane-averaged value of $\phi$ |
| $\tilde{\phi}$ | dispersion of $\phi$: $\phi - [\phi]$ |
| $\phi^+$ | normalized $\phi$ by the friction velocity |

## 1. Introduction

From the engineering viewpoint, walls are not always hydraulically smooth but have roughness and/or permeability. Since such wall roughness and permeability significantly change turbulence characteristics and hence engineering device performance, many studies have been carried out to understand the flow physics over such wall surfaces. As summarized in review articles by Raupach et al. (1991); Jiménez (2004); Piomelli (2018), there have been a huge number of experimental and numerical studies dedicating to rough wall turbulence. Among them, early experimental studies (e.g. Nikuradse, 1933; Colebrook and White, 1937; Colebrook, 1939; Moody, 1944) found the correlations between the roughness height and the wall friction or the mean velocity profile. In rough wall turbulent boundary layers, the semi logarithmic portion of the mean velocity profiles shift downward depending on the equivalent sand grain roughness height $k_s$ (Nikuradse, 1933) forming an empirical formula:

$$U^+ = \kappa^{-1} \ln \frac{\hat{y}}{k_s} + 8.5, \tag{1}$$

for fully rough wall flows. Here, $U^+$, $\kappa$ and $\hat{y}$ are the streamwise mean velocity normalized based on the friction velocity, the von Kármán constant and the wall normal distance, respectively. As Jiménez (2004) noted, it is necessary to determine the origin for $\hat{y}$ for rough walls and a shift (zero-plane displacement) from some reference location is usually determined empirically. Equation (1) can be rewritten as

$$U^+ = \kappa^{-1} \ln \hat{y}^+ + 5.1 - \Delta U^+, \tag{2}$$

where $\Delta U^+$ is the so-called roughness function and written as

$$\Delta U^+ = \kappa^{-1} \ln k_s^+ - 3.4. \tag{3}$$

After extensive measurements of rib-roughened turbulent boundary layer flows, Perry et al. (1969) categorized the roughness into two types: k- and d-types, which are distinguished by the ratio of the roughness height and interval. The letters "k-" and "d-" respectively correspond to the roughness height and the boundary layer thickness which are characteristic length scales determining the roughness function and the friction factor. For the regularly spaced rib-roughness, it was reported that the demarcating ratio of the rib-interval to the rib-height was $\lambda/k = 4$ (Tani, 1987). In the turbulent flows over the k-type roughness at $\lambda/k > 4$, there are recirculation vortices that reattach ahead of the next roughness elements, hence exposing them to outflows (Cui et al., 2003; Leonardi et al., 2003; Ashrafian et al., 2004). Also, it is known that the roughness function becomes maximum when $\lambda/k = 8$ (Flack and Schultz, 2014). On the other hand in the d-type roughness at $\lambda/k < 4$, the roughness function becomes independent of the roughness height (rod-height) $k$. Over such d-type roughness, there are stable recirculation vortices that isolate the outer flow from the roughness (Cui et al., 2003; Leonardi et al., 2003, 2004). These different phenomena affect turbulence characteristics over the roughness.

As for turbulence over permeable porous walls, many experimental studies (e.g. Lovera and Kennedy, 1969; Ruff and Gelhar, 1972; Ho and Gelhar, 1973; Zagni and Smith, 1976; Zippe and Graf, 1983; Kong and Schetz, 1982; Shimizu et al., 1990; Pokrajac and Manes, 2009; Manes et al., 2009; Detert et al., 2010; Suga et al., 2010; Suga, 2016; Manes et al., 2011) revealed the fact that the permeability enhances momentum exchange across the surfaces and modifies the near-wall turbulent flow structure. Since the permeability relaxes the near-wall damping effects on vortex motions, turbulence is allowed to maintain its strength even on the surface (Suga et al., 2010, 2011). The direct numerical simulation (DNS) studies of Breugem et al. (2006); Kuwata and Suga (2016) and the particle image velocimetry (PIV) experiments of Suga et al. (2010, 2017) for turbulent channel flows over isotropic porous media suggested that there were correlations between the inner turbulence characteristics and the permeability Reynolds number which is based on the friction velocity $u_\tau^{\mathrm{p}}$ on the porous wall, the wall permeability $K$ and the fluid kinematic viscosity $\nu$. In particular, for the semi logarithmic portion of the mean velocity profiles

$$U^+ = \kappa^{-1} \ln \frac{\hat{y} + d_0}{h}, \tag{4}$$

the parameters: $\kappa$, the zero-plane displacement $d_0$ and the roughness scale $h$, could be characterized by the permeability Reynolds number (Suga et al., 2010; Manes et al., 2011; Suga et al., 2017). Although equation (4) is essentially the same as equation (1), such a formula is usually applied to the flows over porous media and canopies (Best, 1935; Nikora et al., 2002; Nepf and Ghisalberti, 2008). Breugem et al. (2006); Suga et al. (2017, 2018) also confirmed that the turbulent streaks were destroyed over highly permeable walls due to the downwash motions into the wall induced by the Kelvin-Helmholtz (K-H) instability. This K-H instability is generated by the inflection of the mean velocity profile underneath the porous surface (Jiménez et al., 2001).

Generally, the surface structures of porous media are not always flat. For example, the surfaces of river beds and urban canopies, which are usually considered as porous media, should not be flat. Recent high performance heat sinks apply porous materials for the finned structures. Furthermore, the rib roughened cooling passages for turbine blades try to apply porous materials to avoid hot spots behind the riblets and to reduce the pressure drops (Panigrahi et al., 2008; Wang et al., 2010; Nuntadusit et al., 2012). Accordingly, flows over permeable roughness should be discussed to understand the engineering wall turbulence more deeply. However, to the best of the authors' knowledge, turbulent flows over permeable rough walls have never been systematically discussed. Therefore, to understand the combined effects of the structural roughness and the wall permeability, we perform planar PIV measurements of turbulent flows in a channel with a porous bottom wall roughened by transverse square rods at the bulk Reynolds numbers of $Re_b$=5000–20000. The chosen roughness structure is the k-type roughness with $\lambda/k = 10$ since this specific k-type roughness was studied in details by many researchers such as Hanjalić and Launder (1972); Cui et al. (2003); Leonardi et al. (2003); Ikeda and Durbin (2007). Note that when permeability effects are included, the turbulence characteristics might not be necessarily categorized in the k-type roughness. Three kinds of isotropic porous media whose porosity is $\varphi = 0.8$ with different permeabilities are applied to both the transverse rods and bottom walls. To make the effects of permeable rods clearer, solid impermeable rods are also considered for the rib-roughened porous walls.

## 2. Experimental method

Fully developed turbulent channel flows over rib-roughened porous surfaces are considered in this study. Fig. 1 shows the experimental set-up and the coordinate system in the test section. The flow facility consists of a water tank, a conditioning tank with a nozzle and a flow channel for the measurement whose geometry is shown in Fig. 1(a). Deaerated tap water is pumped up from the water tank and led to the conditioning tank containing a honeycomb-bundled section, where the water temperature is recorded by a digital thermometer (FD-T1, KEYENCE). Then the flow is developed in the 3.0 m long driving section and enters the 1.0 m long test section. The water channel has a sectional area of 0.3 m (width)$\times$0.06 m (height) and is filled by the porous slabs up to the bottom half of the channel as shown in Fig. 1(b). Since the height of the clear channel region is $H = 0.03$ m, the aspect ratio of the cross section of the clear flow region is about 10 and two-dimensionality of the flow field was confirmed in the range of $\pm 2H$ from the symmetry plane by our previous study (Suga et al., 2013) for rib-roughened flows and hence the measurements are carried out in the symmetry plane of the channel. The range of the measured bulk Reynolds number $\mathrm{Re}_b = U_b H/\nu$ is 5000 – 20000 which reach the lower operating range of turbine-blade cooling channels (Han et al., 1985). Here, the bulk mean velocity $U_b$ is obtained by integrating the measured cross-sectional streamwise mean velocity distribution over the porous wall.

On the porous wall, transverse square rods whose sectional area is $3 \times 3$ mm$^2$ are placed with a regular pitch at $\lambda$ =30 mm (Fig.1(d)). Both acrylic impermeable and porous rods, are applied to see the effects of the rod permeability. For the porous rods, the same porous structure as that for the bottom wall is applied to consider naturally roughed porous surfaces. Since the height of the square rods is 3 mm, the maximum pore diameter for the rods should be less than 3 mm. Correspondingly, the maximum mean pore diameter $D_p$ of the porous medium is 2.8 mm in porous medium #13 as listed in Table 1. To see the effects of the different porous media, we choose two other porous media #20 and #30 whose mean pore diameters are $D_p =$ 1.7 and 0.9 mm which are approximately 2/3 and 1/3 of the rod height $k$ as shown in Table 1. They are foamed ceramics (Ceramic Foam, Bridgestone) having isotropic open-cell foam structures of nearly the same porosity $\varphi = 0.8$. Table 1 also lists the permeability $K$ and Forchheimer coefficient $C^F$. By measuring flow rates and pressure drops $\Delta P$ along the distance $\Delta x$, our previous study (Suga et al., 2010) obtained them through the classical Darcy-Forchheimer equation:

$$-\frac{\Delta P}{\Delta x} = \frac{\mu U_d}{K} + \frac{C^F}{K}\rho U_d^2, \tag{5}$$

where $\mu, \rho$ and $U_d$ are the fluid viscosity, density and the mean velocity, respectively. Since the permeability of porous medium #13 is more than eight times larger than that of porous medium #30 while their porosities are nearly the same, we can see the effects of approximately one order different permeabilities irrespective of the porosity. The measured flow cases in the present study are summarised in Tables 2 and 3 with parameters which are obtained by the analyses discussed in later sections. The solid rib flow case over #xx porous wall is named case #xxs while the porous rib flow case is named case #xxp. Case solid in Table 2 is the solid rib flow over the impermeable smooth wall.

The applied planar PIV system consists of a Nd-Yag Laser (Dual Power 200-15, Litron) with 200 mJ per pulse at a wavelength of 532 nm and a CCD camera (Flowsence 4M MkII, DANTEC DYNAMICS) operating at 30 fps (frames per second) with 85 mm $f/1:8$ lenses (AF Nikkor, Nikon) to cover a section of $33(x) \times 33(y)$ mm$^2$ with 2048×2048 pixels$^2$. For the measurements, the laser beam is formed into a sheet of approximately 1.0 mm thickness by several cylindrical lenses and illuminates the measuring domain as illustrated in Fig. 1(c). The size of the interrogation windows, which overlap 50% in each direction, is set to 32×32 pixels$^2$. Accordingly, 127×127 vectors are produced for each image pair. In the present study, 5000 image pairs, whose time intervals are $140-550$ $\mu s$, are recorded with a sampling rate of $4-5$ Hz for each case. The average particle displacement was set to be approximately 25 % of the interrogation window size ($6-8$ pixels). The recorded data are processed by Dynamic Studio 2015a (DANTEC DYNAMICS). When the ratio of the first and second correlation peaks in each interrogation window is smaller than 1.3, it is removed from the process as an error vector. Furthermore, the moving-average validation (Host-Madsen and McCluskey, 1994) is applied with an acceptance factor of 0.1.

For the tracer particles, acrylic colloid particles are used. Their mean diameter and specific gravity are 3.1 $\mu$m and 1.19, respectively. By the use of image processing software, the average number of pixels for a particle image captured by the CCD camera is counted to be about $3-4$ pixels. According to the discussions of Prasad et al. (1992), this indicates that the particle images are well resolved in the present experiments, and the uncertainty in the measured displacement is expected to be approximately less than 1/10 of the diameter of the particle image. Normalizing this uncertainty by the mean displacement length of particles indicates that the estimated error of the instantaneous velocity is less than 4% of the maximum velocity in the frame.

## 3. Results and discussions

### 3.1. Solid-rod roughened cases

#### 3.1.1. Mean flow profiles

To see general ideas of the flow fields, Fig. 2 shows the streamlines for the cases with solid rods (or ribs) such as cases solid, #30s, #20s and #13s at $\mathrm{Re}_b \simeq 5000$ and 15000. They are produced by plotting contour lines of the stream functions calculated with the measured mean velocity distributions. As seen in Fig. 2(a-d), large recirculation bubbles behind the solid rib exist. Due to the inevitable smoothing effect (which appears when there is a large velocity difference within an interrogation window) of the PIV measurements close to the walls, unreliable near-wall velocity data cannot be used. Hence, extrapolation of the line indicating $\overline{u} = 0$ to the wall is applied to estimate the reattachment and the separation points. For case solid at $\mathrm{Re}_b$=5000, the estimated reattachment length is $X_R \simeq 5.1k$ which is consistent with the data in the literature. See Fig.1(d) for the illustrative definition of the reattachment point $X_R$. Indeed, Leonardi et al. (2003); Liu et al. (1966) reported that their reattachment lengths are $X_R \simeq 4.8k$ and $5k$ for $\lambda/k \simeq 8$ and $\lambda/k \simeq 8, 12$, respectively. Leonardi et al. (2003) also reported that the flow separates from $1.5k$ before the next rib. The corresponding position in the present case solid is $1.8k$ which reasonably agrees with that of Leonardi et al. (2003). In case #30s, the recirculation region looks submerged to the wall due to the wall permeability. The reattachment length in this case at $\mathrm{Re}_b = 5400$ is $X_R \simeq 4.7k$ which is slightly shorter than the case solid. As $\mathrm{Re}_b$ increases, $X_R$ becomes shorter as $X_R \simeq 4.0k$. As the wall permeability increases, in case #20s and #13s as shown in Fig. 2(e, f, g, h), the recirculation bubbles are expanded and submerged further resulting in vanishing of the reattachment point. Table 2 lists $X_R$ for each case.

To examine the flow field more in details, Fig. 3 compares the mean velocity distribution profiles of cases #solid, #30s, #20s and #13s at $x/k$ =0.5, 2.5, 4.5, 6.5 and 8.5 for $\mathrm{Re}_b \simeq 15000$. As shown in Fig. 3(a), the streamwise mean velocity $\overline{u}$ at $x/k = 0.5$ for permeable wall cases become small at $y/H \leq 0.3$ compared with case solid. The same trend can be seen at $x/k = 2.5$ over $y/H = 0.1$ although the reverse flow at $y/H \leq 0.1$ becomes weak as the wall permeability increases. This is because the low pressure region behind the rib is weakened by the entrainment of the fluid flow from the porous layer and the recirculation vortex shrinks as seen in the flow pattern in Fig. 2. This flow phenomenon is similar to the "by-passing" flow which was observed in a rib-mounted porous walled channel flow by Suga et al. (2013). (Due to the rib blockage, a part of the blocked fluids goes through the porous wall under the rib and springs out from the wall behind the rib. Suga et al. (2013) called such a phenomenon the by-passing flow.) They reported the enhancement of the by-passing flow as the increase of the wall permeability. Accordingly, the amount of the flow rate over the rib becomes small as the wall permeability increases. As shown in Fig. 3(b), the absolute magnitude of the wall-normal mean velocity $\overline{v}$ becomes small at $y/H \leq 0.6$ as the wall permeability increases since the recirculation vortex becomes weak. As observed in Fig. 2(f), due to the flow coming through the wall, near-wall $\overline{v}$ at $x/k = 4.5$ in case #13s becomes clearly positive.

Fig. 4 shows the turbulence statistics of cases solid, #30s, #20s and #13s at $\mathrm{Re}_b \simeq 15000$. The streamwise, wall-normal root mean square (rms) velocities and Reynolds shear stress become smaller as the wall permeability increases (case solid $\rightarrow$ case #30s $\rightarrow$ case #20s $\rightarrow$ case #13s). This is because the shear layer behind the rib becomes weaker due to the entrainment of the by-passing fluids. At $x/k = 8.5$,the magnitude of the near-wall $v'_{\mathrm{rms}}$ (Fig. 4(b)) becomes slightly larger in porous wall cases. Corresponding to this $v'_{\mathrm{rms}}$ profile, the near-wall shear stress at $x/k = 8.5$ also becomes larger depending on the wall permeability. According to the DNS results of turbulent flows in symmetric rib-roughened channel (Ashrafian et al., 2004), the effects of the rib are limited to $5k$. Moreover, Raupach et al. (1991) reported that roughness has a profound influence on the turbulence structure in a layer whose depth is $3k - 5k$. As seen in Figs. 3 and 4, the turbulent intensities seems to be affected by the roughness all over the flow region although the mean velocity distribution looks consistent with their reports.

### *3.1.2. Quadrant analysis*

To understand the local characteristics of turbulence close to the wall, the Reynolds shear stress is decomposed into the quadrant events: $\mathrm{Q}m = \Sigma(u'v')_m/\Sigma N_m$, where subscript $m(= 1 - 4)$ and $N_m$ correspond to each quadrant event and its processed number. Fig.5 (a, b, c) shows the distributions of the quadrant events of cases solid, #30s and #13s at $y/k \simeq 0.33$ for $\mathrm{Re}_b \simeq 15000$. It is seen that Q4 (sweeps) is generally the strongest followed by Q2 (ejections) between the ribs while Q1 and Q3 are significantly smaller than those in all cases. Just behind the rib at $1 < x/k < 2.5$, the growth rate of each event of cases #30s and #13s is smaller than that of case solid. As the wall permeability increases, the growth rate tends to be smaller as clearly seen in Fig.5 (a-c). This trend corresponds to the locations of the recirculation bubbles shown in Fig.2. Since the recirculation bubble centre shifts downstream as the wall permeability increases, turbulent shear behind the rib tends to be weakened. In the region $x/k > 9$ shown in Fig.5 (a), the magnitude of each event in case solid increases again to attain the second local maximum/minimum while such a trend is not obvious in cases #30s and #13s. It is known that there is another small recirculation in front of the rib face in case solid (although it is not obvious in Fig.2), correspondingly larger turbulent shear takes place there. However, with the wall permeability, a part of the blocked fluid by the rib passes through the bottom wall under the rib resulting in the relaxation of the velocity gradient and thus shear generation.

Fig.5 (d) compares the profiles of Q4. It is clear that the location of the upstream local minimum (negative peak) shifts downstream and the negative peak profile tends to be flatter in the permeable wall cases. This indicates that a relatively larger area of the wall surface is exposed to stronger sweep events in the permeable wall cases. This is because the permeable surface relaxes the wall blocking to the sweep motions and more sweep motions are able to approach the wall surface.

*3.1.3. Plane averaged mean flow profiles*

To see the effects of the Reynolds number, Figs. 6 and 7 compare the streamwise averaged turbulence statistics of case solid at $\mathrm{Re}_b = 5000 - 20600$, case #30s at $\mathrm{Re}_b = 5400 - 14100$, case #20s at $\mathrm{Re}_b = 4800 - 21000$ and case #13s at $\mathrm{Re}_b = 5000 - 20300$. In those figures $[\cdot]^f$ denotes a fluid phase streamwise averaged value. Although the experiments are performed only in the symmetry plane of the channel, the streamwise averaged values are called "$x - z$ plane averaged" values in this study hereafter since two-dimensionality of the measured section in this flow facility was assured (Suga et al., 2013). The streamwise and wall-normal velocity dispersions and the dispersion shear stress:

$$\sqrt{[\tilde{\bar{u}}\tilde{\bar{u}}]^f} = \sqrt{\frac{1}{\lambda^f}\int_0^{\lambda}\left(\bar{u} - [\bar{u}]^f\right)^2 dx^f}, \tag{6}$$

$$\sqrt{[\tilde{\bar{v}}\tilde{\bar{v}}]^f} = \sqrt{\frac{1}{\lambda^f}\int_0^{\lambda}\left(\bar{v} - [\bar{v}]^f\right)^2 dx^f}, \tag{7}$$

$$[\tilde{\bar{u}}\tilde{\bar{v}}]^f = \frac{1}{\lambda^f}\int_0^{\lambda}\left(\bar{u} - [\bar{u}]^f\right)\left(\bar{v} - [\bar{v}]^f\right) dx^f, \tag{8}$$

are also plotted. Here, superscript "$f$" denotes fluid phase value and $\lambda^f = \int_0^{\lambda} dx^f$. As seen in Figs. 6 and 7, the profiles of the mean velocity look almost the same regardless of the Reynolds numbers. However, the wall-normal components of the turbulent intensity and the Reynolds shear stress at $\mathrm{Re}_b \simeq 5000$ show slightly deviated values from those at the other $\mathrm{Re}_b$ cases while the other variables reasonably collapse to single profiles as in the mean velocity. This corresponds to the size of recirculation bubble at $\mathrm{Re}_b \simeq 5000$ which is slightly larger than those of the higher $\mathrm{Re}_b$ cases as shown in Fig. 2.

For the discussion on the general effects of the wall permeability, Fig. 8 compares the plane averaged turbulence statistics of cases #solid, #30s and #13s at $\mathrm{Re}_b \simeq 15000$. Although the flow pattern significantly changes depending on the wall permeability as seen in Fig. 2, it is interesting that the plane averaged mean velocities shown in Fig. 8(a) do not change so significantly. This result suggests that the effect of the solid ribs is more influential to the mean velocity distribution than the effect of the wall permeability. However, as for the rms velocities (turbulent intensities) and Reynolds shear stress in Fig. 8(b-d), it is obviously observed that they become lower as the wall permeability increases. In particular, the streamwise turbulent intensity becomes significantly smaller compared with the wall-normal component. This implies that turbulence becomes less anisotropic due to the wall permeability.

The velocity dispersions in Fig. 8(e, f) also become smaller as the wall permeability increases while the dispersion stresses in Fig. 8(b) only show difference under the rib top at $y/H \leq 0.1$. It is worth noting that although the profiles of the streamwise dispersion $\sqrt{[\tilde{\tilde{u}}\tilde{\tilde{u}}]^f}$ and the wall-normal dispersion $\sqrt{[\tilde{\tilde{v}}\tilde{\tilde{v}}]^f}$ at $y/H \geq 0.5$ have almost the same magnitudes for all cases, they change significantly near the rib.The magnitudes at $y/H \leq 0.3$ of porous cases become smaller as the wall permeability increases. The influence of permeability on the velocity dispersion can be seen more clearly in the profile of the wall-normal dispersion in Fig. 8(f). For cases solid and #30s, the magnitudes become smaller towards the bottom wall while for case #13s the profile at $y/H \leq 0.05$ becomes large. This is because of the enhancement of the by-passing flow and the flow into the porous wall in front of the rib depending on the permeability.

### *3.2. Porous-rod roughened cases*

#### *3.2.1. Streamlines*

To see the rib permeability effects, Fig. 9 describes the streamlines of cases #30p, #20p and #13p at $\mathrm{Re}_b \simeq 5000, 15000$. Compared with the solid rib cases shown in Fig. 2, the upstream edge of the recirculation bubble moves downstream due to the flow through the porous rib. Also, the size of the recirculation bubble at $\mathrm{Re}_b$ =15300 of case #30p in Fig. 9(b) looks smaller than the plots at $\mathrm{Re}_b$ =5000 in Fig. 9(a). This trend is the same as that seen in the solid rib cases. As the Reynolds number increases it is seen that the centre position of the recirculation bubble moves downstream and downward. For the porous rib cases, the location at which the flow separation occurs does not correspond to the downstream edge of the rib-top surface. The flow separates a little downstream from the rib back-face and thus the front of the separation bubble is $X_F = 2.0k$ for case #30p at $\mathrm{Re}_b = 5000$. See Fig.1(d) for the illustrative definition of the front location of the separation bubble $X_F$. We estimate $X_F$ from the distribution of $\bar{u} = 0$ as we do for $X_R$. The flow reattachment length is $X_R = 5.6k$. Correspondingly, the size of the bubble $X_R - X_F$ appearing over the surface is approximately $3.6k$. As listed in Table 3, $(X_R - X_F)$ becomes smaller as Reynolds number increases. When the permeability increases for cases #20p and #13p, the recirculation bubble disappears and flow separation and reattachment are no longer seen.

*3.2.2. Quadrant analysis*

Fig.10 (a, b) shows the magnitude of each quadrant event for $\mathrm{Re}_b \simeq 15000$ at $y/k \simeq 0.33$ in cases #30p and #13p. Although the general tendency is similar to that of solid rib cases (shown in Fig.5), it is clear that there are events even just behind the rib and their magnitudes are larger in case #13p (larger permeability case). Fig.10 (c) compares the profiles of Q4 in cases #30p, #13p and #13s (solid rib). It can be seen that the magnitude behind the rib increases for the porous rib cases depending on the permeability. This clearly indicates that some vortex motions are not blocked on the porous rib surface and shear generation maintains such a certain level. Although the profiles at $3 < x/k < 6$ are almost the same, the magnitudes for porous rib cases become slightly smaller than that of case #13s (solid rib) at $6 < x/k < 10$. This indicates that the strength of the sweeps in the downstream region is slightly relaxed by the porous rib effect. Due to the blockage effect of the solid rib, more amount of the fluid tends to go through the bottom wall resulting in such an enhanced sweep profile.

*3.2.3. Plane averaged mean flow profiles*

Fig. 11 shows the turbulence statistics of cases #30p, #20p and #13p at $\mathrm{Re}_b \simeq 5000 - 20000$. The plane averaged mean velocities in Fig. 11(a-c) look insensitive to $\mathrm{Re}_b$ and this trend is similar to that seen in the solid rib cases in Figs. 6 and 7. Also, the general trends of the other turbulence quantities show similar tendencies to those seen in the solid rib cases. They are slightly larger at $\mathrm{Re}_b \simeq 5000$ than those at $\mathrm{Re}_b \simeq 10000 - 20000$.

To see the effect of the rib permeability, Fig. 12 compares the turbulence statistics of the solid and porous ribs: cases #13s and #13p. As shown in Fig. 12(a), the mean velocity below the rib top: $y/H \leq 0.1$, obviously becomes larger in the porous rib case due to the flow through the porous rib. This results in the slightly lower peak profile at $y/H \simeq 0.75$. As for the turbulent intensities in Fig. 12(c,d), generally the level becomes smaller in case #13p compared with that in case #13s. This is because the strength of the recirculation becomes weaker due to the flow through the porous rib. The same tendency is also seen in the profiles of the Reynolds shear stress in Fig. 12(b). As for the velocity dispersion shown in Fig. 12(c, d), corresponding to the change of the general flow profiles shown in Figs. 2 and 9, the wall-normal velocity dispersion becomes small at $y/H \leq 0.4$ in the porous rib case. Under the rib top $y/H \leq 0.1$, the profiles of the velocity dispersions and the dispersion shear stress (Fig. 12(b)) of the porous rib case show a smaller magnitude since the porous rib weakens the recirculation.

To discuss the combined effect of the wall and rib permeability, Fig. 13 compares the turbulence statistics of cases #30p, #20p and #13p. As shown in Fig. 13(a), the mean velocity below the rib top at $y/H \leq 0.1$ becomes large as the wall permeability increases. This is because of the flows through the porous ribs. As seen in Fig. 13(b-d), the turbulent intensities and the Reynolds shear stress generally become smaller as the wall permeability increases. This trend is opposite to that of the rib-less cases in which turbulence becomes larger depending on the increase of the permeability (Suga et al., 2010, 2017). This implies that turbulence generated by the rib solidity is more influential than the permeability induced turbulence. As for the dispersion stress, as shown in Fig. 13(b) the difference between the cases looks marginal. However, as shown in Fig. 13(e, f) the streamwise and wall-normal velocity dispersions generally become smaller as the permeability increases at $y/H > 0.1$. Since the porous wall and ribs weaken the recirculation behind the ribs, the mean velocity distributions are relaxed resulting in the smaller velocity dispersions as the permeability increases.

### *3.3. Zero-shear stress and maximum mean velocity locations*

In asymmetric rough wall channel flows, the zero-shear stress location $y_0 = y|_{\overline{u'v'}=0}$ does not coincide with the maximum mean velocity location $y_m = y|_{[\overline{u}]^f=[\overline{u}]^f_{max}}$, which was pointed out by Hanjalić and Launder (1972). Their geometry for $\lambda/k = 10$ indicated $y_0/H \simeq 0.83$ and $y_m/H \simeq 0.75$ while for the same geometry Ikeda and Durbin (2007) simulated as $y_0/H = 0.81$ and $y_m/H = 0.76$.

As shown in Fig.14(a), the present case solid shows $y_0/H = 0.8 - 0.82$ which is close to the data cited above. The increasing trend depending on $\mathrm{Re}_b$ is consistent with the data of Hanjalić and Launder (1972). As for $y_m$ shown in Fig.14(b), case solid shows $y_m/H \simeq 0.76$ that is almost constant while Hanjalić and Launder (1972) measured values increasing with $\mathrm{Re}_b$. When the bottom wall has permeability, it is generally seen that both $y_0$ and $y_m$ tend to be smaller and they become further smaller with the porous rib while $y_0$ is always larger than $y_m$. It is considered that the permeability of the wall and the rib makes the roughness effect weakened and thus the flow becomes less asymmetric. This indicates that the drag on the rough surface tends to be smaller as the wall and rib permeability increases.

### 3.4. Log-law fitting

To discuss near-wall (inner layer) turbulence, we normally apply the friction velocity as a representative velocity scale. However, it is not easy to obtain it in rough and permeable wall flows. For the estimation of the friction velocity on a rough wall, the conventional way is fitting a mean velocity profile to Eq.(1) with the von Kármán constant $\kappa \simeq 0.42$. By such log-law fitting, both the friction velocity and the equivalent sand grain roughness are estimated. Although there are several ways to determine the origin of the wall-coordinate $\hat{y}$, we determine it at the rib top $y = k$. (However, the location of the origin does not essentially affect the following discussion.) For case solid, the semi-logarithmic profiles with fitting lines of Eq.(1) are plotted in Fig. 15(a). Note that $[\bar{u}]^{f+} = U^+$ in the log-law formulas and the displacement of $0.9k$ which corresponds to the mean roughness height $(0.1k)$ is applied to the abscissa in Fig. 15(a). The obtained friction velocity and equivalent sand grain roughness by this method are listed in Table 4 denoting as $u_*^N$ and $k_s^N$, respectively.

In the porous wall flows, it is known that the von Kármán constant varies depending on the Reynolds number (Breugem et al., 2006; Manes et al., 2011; Suga et al., 2010, 2017, 2018). In such a case, to fit the log-law line, Breugem et al. (2006); Suga et al. (2010) described the detailed procedure to obtain $\kappa$, $d_0$ and $h$ for Eq.(4). However, to follow their procedure, it is necessary to pre-determine the friction velocity $u_*$. As Pokrajac et al. (2006) discussed, it has been controversial to determine the friction velocity since there are several candidates for the reference shear stress such as the bed shear stress, the total fluid shear stress at the roughness crest, etc. Note that the total fluid shear stress is the sum of the plane averaged viscous, Reynolds and dispersion shear stresses. Following Finnigan (2000); Poggi et al. (2004); Jarvela (2005); Nakagawa et al. (1991); Pokrajac et al. (2006); Coceal et al. (2007), this study defines $u_*$ from the total fluid shear stress at the roughness crest (rib top location: $y = k$). We estimate it by extrapolating the profile of the sum of the Reynolds and dispersion shear stresses to the rib top location since measuring the viscous shear stress accurately in the vicinity of the solid surfaces is difficult.

For case solid, as listed in Table 4 the estimated $u_*$ by the above mentioned way is a little smaller than $u_*^N$. With those $u_*$, log-law fitting to Eq.(4) is performed. Fig. 15(b) shows the mean velocity distributions for cases solid, #30s and #13s at $\mathrm{Re}_b \simeq 15000$. For case solid, irrespective of $\mathrm{Re}_b$ the displacement $d_0$ from the fitting to Eq.(4) becomes $d_0 \simeq 0.9k$ which corresponds to the mean roughness height mentioned above. In Fig. 15(b), it is seen that the slope of the logarithmic region becomes steeper as the wall permeability increases. This is consistent with the turbulent flows over rib-less porous walls (Suga et al., 2010, 2017). Moreover, it is found that $d_0$ and the roughness scale $h$ become larger as the wall permeability increases as shown in Table 2.

Fig. 16 shows the fitted logarithmic profiles for cases solid, #30s, #30p, #20s, #20p, #13s and #13p at $\mathrm{Re}_b \simeq 5000 - 20000$. The obtained three parameters $\kappa$, $d_0$ and $h$ are listed in Tables 2 and 3. Fig. 17 indicates their distributions against $\mathrm{Re}_\tau$ which is defined as $\mathrm{Re}_\tau = u_\tau^R \delta/\nu$ where $\delta = y_m$ and $u_\tau^R = \sqrt{\tau^R/\rho}$. See Appendix for the estimation process of the total drag $\tau^R$ on the rough wall. As seen in Fig. 17(a), for case solid, $\kappa$ is almost constant as $\kappa \simeq 0.41$ while it becomes smaller as the wall permeability increases for the solid and porous rib cases. For cases #30s and #30p, $\kappa$ becomes slightly smaller as $\mathrm{Re}_\tau$ increases while it tends to be constant in higher permeability cases. As for the zero plane displacement $d_0$ shown in Fig. 17(b), $d_0^+$ of case solid almost perfectly accords with $0.9k$ which corresponds to the mean roughness hight as mentioned above. As the permeability and Reynolds number increase, $d_0^+$ tends to be larger. This indicates that turbulent vortices penetrate across the porous interface more deeply as the permeability and Reynolds number increase. Furthermore, it is interesting that the deviation of the levels in the solid rib cases #30s – #13s is smaller than that in the porous rib cases #30p – #13p. This indicates that the rib permeability is significantly influential to the displacement. The distribution of the roughness scale $h^+$ shown in Fig. 17(c) also shows the general trend that $h^+$ becomes large as $\mathrm{Re}_\tau$ and the permeability increase. It is seen that the deviations of the $h^+$ profiles in the solid and porous rib cases look similar. The characteristics of the roughness scale are further discussed in terms of the equivalent sand grain roughness in the next section.

### *3.5. Equivalent sand grain roughness and roughness function*

When the displacement is introduced to Eq.(1) (or we replace $\hat{y}$ with $\hat{y} + d_0$ in Eq.(1)) and compared with Eq.(4), we can obtain the equivalent sand grain roughness $k_s^+$ as

$$\ln k_s^+ = \ln h^+ + 8.5\kappa. \tag{9}$$

Then, the roughness function $\Delta U^+$ is obtainable by Eq.(3). The obtained $k_s^+$ values are compared in Fig. 18(a). The red line indicates $k_s^{N+}$ by Eq.(1)

listed in Table 4. It is clear that the present $k_s^+$ profile of case solid do not agree with the red line. However, the blue chain line which corresponds to the values for case solid obtained with $u_\tau^R$ instead of $u_*$ well accords with the red line. This confirms that the traditional scheme corresponds to the present scheme when the total drag on the bottom surface (bed shear stress) is applied instead of the shear stress at the roughness crest. For all cases, it is seen that the profiles of $k_s^+$ become large almost linearly as the Reynolds number increases.

Fig. 18(b) compares the roughness function $\Delta U^+$ against $k_s^+$. The red line indicates the Nikuradse-type roughness function for uniform sand roughness by Schlichting (1979). Obviously, plots of case solid well collapse to the red line while plots of porous cases are significantly higher than the line and become larger as the permeability increases.

For comparison of the total drag, the drag coefficient defined as $c_D \equiv 2\tau^R/(\rho U_b^2)$ are plotted in Fig. 19. As for the general tendency, $c_D$ becomes small as the permeability increases for both the solid and porous rib cases. This results from the weakening of the recirculation bubbles behind the ribs due to the permeability. Although $c_D$ decreases almost linearly in case solid as the Reynolds number increases, the decreasing rates in porous cases look saturated at $\mathrm{Re}_b > 10000$.

## 4. Concluding remarks

Particle image velocimetry measurements are performed for the turbulent k-type rib-roughened porous channel flows at the bulk Reynolds number of $\mathrm{Re}_b$ =5000 − 20000. Solid impermeable and porous rods are considered for the rib-roughness whose pitch/rib-height is $\lambda/k = 10$. Three kinds of isotropic porous media with nearly the same porosity: $\varphi = 0.8$, and different permeabilities ($K$ =0.004, 0.020, 0.033 mm$^2$) are applied. The concluding remarks from the present study are:

(1) The recirculation bubble appearing between the ribs becomes small submerging into the porous wall and eventually vanishes as the wall permeability increases for both solid and porous rib cases. This trend is further enhanced in the porous rib cases and characterises the turbulence quantities.

(2) It is confirmed that the zero-shear stress location does not coincide with the maximum mean velocity location in all cases. When the bottom wall has permeability, it is generally seen that both locations tend to be smaller and they become further smaller with the porous rib while the zero-shear stress location is always larger than the maximum mean velocity location. This indicates that the drag on the rough surface tends to be smaller as the wall and rib permeability increases.

(3) The generalised scheme to fit mean velocity profiles to the log-law form is discussed. When the friction velocity based on the shear stress at the roughness crest is applied, the obtained equivalent sand grain roughness does not agree with that by the traditional Nikuradse method for the solid-rib-roughed solid-wall flows. However, when the bed shear stress is applied, they agree well. This confirms that the shear stress obtained by the traditional fitting method corresponds to the bed shear stress.

(4) By fitting the mean velocity profiles to the log-law form, it is confirmed that the zero-plane displacement increases while the von Kármán constant and the equivalent sand-grain roughness decrease as the wall and

rib permeability increases.

(5) The drag over the rib-roughed wall becomes small as the permeability increases for both the solid and porous rib cases because the weakening of the recirculation bubbles behind the ribs. Although the drag coefficient decreases as the Reynolds number increases, the decreasing rates in the porous cases tend to be saturated at $\mathrm{Re}_b > 10000$.

**Acknowledgements**

A part of this study was financially supported by the research grant (No.19H02069) of the JSPS.

**Appendix: Estimation of the total drag (bed shear stress)**

By the double (time and volume) averaging, the force balance of the rough-wall channel flow may be written as

$$-H\frac{d\langle\bar{p}\rangle}{dx} = \tau^R + \tau^t, \tag{10}$$

where $\langle\bar{p}\rangle$, $\tau^R$ and $\tau^t$ are the double averaged pressure, the total drag on the rough wall (bed shear stress) and the top-wall viscous drag, respectively. Here, the volume averaging is applied to the entire domain spanning between $x = x_0$ and $x_b$ shown in Fig. 1 (d). When the pressure drop is known, we can easily estimate the total drag by Eq.(10). Otherwise, we have to find another way to estimate the total drag. This is the case in this study.

For the k-type roughness schematically shown in Fig. 1 (b)(d), $\tau^R$ is the sum of the averaged viscous drag $\tau_w$, form drag $\tau_d$ and viscous drag by the flow through the porous rib $\tau_p$. They are defined as

$$\tau_w = \frac{1}{\lambda dz}\int_{C+R}\left(\mu\frac{\partial\overline{u}}{\partial y} - \rho\overline{u'v'} - \rho\bar{u}\bar{v}\right)\boldsymbol{j}\cdot d\boldsymbol{s}, \tag{11}$$

$$\tau_d = \frac{1}{\lambda dz}\int_{R}\left(-\bar{p} + \mu\frac{\partial\overline{u}}{\partial x}\right)\boldsymbol{i}\cdot d\boldsymbol{s}^s, \tag{12}$$

$$\tau_p = \frac{-1}{\lambda dz}\int_{R}\frac{\partial}{\partial y}\left(\mu\frac{\partial\bar{u}}{\partial y} - \rho\overline{u'v'} - \rho\bar{u}\bar{v}\right)dv^f, \tag{13}$$

where $\boldsymbol{i}$ and $\boldsymbol{j}$ are the unit vectors of the streamwise and wall-normal direction, respectively. The surface vector $\boldsymbol{s}$ represents a surface of the regions $C$ and $R$ described in Fig. 1(d). The superscripts "$s$" and "$f$" denote the solid and fluid phases, respectively. Note that although $\rho\overline{u'v'} = 0$ and $\rho\bar{u}\bar{u} = 0$ on solid non-slip walls, it is not the case for porous surfaces and thus Eq.(11) maintains them. For the fully developed flow condition, since $\int_R \frac{\partial\bar{p}}{\partial x}dv + \int_C \frac{\partial\bar{p}}{\partial x}dv = k\lambda dz\frac{d\langle\bar{p}\rangle}{dx}$, Eq.(12) can be rewritten as

$$\begin{aligned}\tau_d &= \frac{1}{\lambda dz}\left(-\int_R \frac{\partial\bar{p^*}}{\partial x}dv^s\right) = \frac{1}{\lambda dz}\left(-\int_R \frac{\partial\bar{p^*}}{\partial x}dv + \int_R \frac{\partial\bar{p^*}}{\partial x}dv^f\right),\\ &= \frac{1}{\lambda dz}\left(\int_C \frac{\partial\bar{p^*}}{\partial x}dv + \int_R \frac{\partial\bar{p^*}}{\partial x}dv^f\right) - k\frac{d\langle\bar{p}\rangle}{dx},\end{aligned} \tag{14}$$

where $\bar{p}^*$ is defined as

$$\bar{p}^* = \bar{p} - \mu\partial\bar{u}/\partial x + \rho\overline{u'u'} + \rho\bar{u}\bar{u}. \tag{15}$$

To obtain the relationship among the drag terms, following Leonardi et al. (2003) the Reynolds averaged Navier-Stokes equation for the streamwise velocity is integrated over the fluid phase of the volume $C$ bounded by consecutive roughness elements as

$$\rho\int_C\left(\frac{\partial\overline{u}\,\overline{u_j}}{\partial x_j} + \frac{\partial\overline{u'u'_j}}{\partial x_j}\right)dv = \int_C\left(-\frac{\partial\bar{p}}{\partial x} + \mu\frac{\partial^2\overline{u}}{\partial x_j^2}\right)dv, \tag{16}$$

which can be rewritten as

$$\begin{aligned} \frac{1}{dz}\int_C \frac{\partial \bar{p^*}}{\partial x} dv &= \int_{x_a}^{x_b} \left( \mu \frac{\partial \bar{u}}{\partial y} - \rho \overline{u'v'} - \rho \bar{u}\bar{v} \right)_{y_b} dx \\ &\quad - \int_{x_a}^{x_b} \left( \mu \frac{\partial \bar{u}}{\partial y} - \rho \overline{u'v'} - \rho \bar{u}\bar{v} \right)_{y_a} dx, \end{aligned} \tag{17}$$

where $y_a$, $y_b$, etc. are shown in Fig. 1(d). The integration of the Reynolds averaged Navier-Stokes equation for the streamwise velocity over the fluid phase of the volume $R$ is

$$\rho \int_R \left( \frac{\partial \bar{u}\ \overline{u_j}}{\partial x_j} + \frac{\partial \overline{u'u'_j}}{\partial x_j} \right) dv^f = \int_R \left( -\frac{\partial \bar{p}}{\partial x} + \mu \frac{\partial^2 \bar{u}}{\partial x_j^2} \right) dv^f, \tag{18}$$

which can be rewritten as

$$\int_R \frac{\partial \bar{p^*}}{\partial x} dv^f = \underbrace{\int_R \frac{\partial}{\partial y} \left( \mu \frac{\partial \bar{u}}{\partial y} - \rho \overline{u'v'} - \rho \bar{u}\bar{v} \right) dv^f}_{-\tau_p \lambda dz}. \tag{19}$$

Note that when the rib material is impermeable, obviously $\int_R \frac{\partial \bar{p^*}}{\partial x} dv^f = 0$. For $\tau_w$, Eq.(11) can be rewritten as

$$\tau_w = \frac{1}{\lambda} \left[ \int_{x_0}^{x_a} \left( \mu \frac{\partial \bar{u}}{\partial y} - \rho \overline{u'v'} - \rho \bar{u}\bar{v} \right)_{y_b} dx + \int_{x_a}^{x_b} \left( \mu \frac{\partial \bar{u}}{\partial y} - \rho \overline{u'v'} - \rho \bar{u}\bar{v} \right)_{y_a} dx \right]. \tag{20}$$

Consequently, using Eqs.(14), (17), (19) and (20), the total drag $\tau^R$ is

$$\begin{aligned} \tau^R &= \tau_d + \tau_w + \tau_p = \frac{1}{\lambda} \int_{x_0}^{x_b} \left( \mu \frac{\partial \bar{u}}{\partial y} - \rho \overline{u'v'} - \rho \bar{u}\bar{v} \right)_{y_b} dx - k \frac{d \langle \bar{p} \rangle}{dx}, \\ &= \mu \frac{\partial [\bar{u}]}{\partial y}\bigg|_{y_b} - \rho \left[ \overline{u'v'} \right]_{y_b} - \rho \left[ \tilde{\bar{u}} \tilde{\bar{v}} \right]_{y_b} - k \frac{d \langle \bar{p} \rangle}{dx}. \end{aligned} \tag{21}$$

where $\frac{1}{\lambda}\int_{x_0}^{x_b} \phi dx$ is the superficial plane averaging and $\frac{1}{\lambda}\int_{x_0}^{x_b} \phi dx = [\phi]$. Note that the plane averaging to $\rho \bar{u}\bar{v}$ produces $[\rho \bar{u}\bar{v}] = \rho[\bar{u}][\bar{v}] + \rho[\tilde{\bar{u}}\tilde{\bar{v}}]$. The plane averaged wall-normal velocity $[\bar{v}]$ is zero and hence only the dispersion shear stress $\rho[\tilde{\bar{u}}\tilde{\bar{v}}]$ remains. With Eq.(10), $\tau^R$ is finally expressed as

$$\tau^R = \frac{1}{H-k}\left\{ H\left( \mu\frac{\partial[\bar{u}]}{\partial y}\bigg|_{y_b} - \rho\left[\overline{u'v'}\right]_{y_b} - \rho\left[\tilde{\bar{u}}\tilde{\bar{v}}\right]_{y_b} \right) + k\tau^t \right\}. \tag{22}$$

Since at $y = y_b$, the superficial averaged values are equivalent to the fluid phase averaged values: $[\cdot] = [\cdot]^f$, we can apply the measured fluid phase plane averaged values to Eq.(22) to obtain the total drag $\tau^R$. However, Eq.(22) can be rewritten as

$$\frac{\tau^R + \tau^t}{H} = \frac{\left( \mu\frac{\partial[\bar{u}]}{\partial y}\Big|_{y_b} - \rho\left[\overline{u'v'}\right]_{y_b} - \rho\left[\tilde{\bar{u}}\tilde{\bar{v}}\right]_{y_b} \right) + \tau^t}{H-k}. \tag{23}$$

which suggests that we can obtain $\tau^R$ by simply extrapolating the profile of the sum of the Reynolds and dispersion shear stresses to the location at $y = 0$.

## References


Ashrafian, A., Andersson, H., Manhart, M., 2004. Dns of turbulent flow in a rod-roughened channel. Int. J. Heat Fluid Flow 25, 373–383.

Best, A.C., 1935. Transfer of heat and momentum in lowest layers of the atmosphere. Technical Report 65. Geophys. Mem., Met. Off. Lond.

Breugem, W.P., Boersma, B.J., Uittenbogaard, R.E., 2006. The influence of wall permeability on turbulent channel flow. J. Fluid Mech. 562, 35–72.

Coceal, O., Dobre, A., Thomas, T., Belcher, S., 2007. Structure of turbulent flow over regular arrays of cubical roughness. J. Fluid Mech. 589, 375–409.

Colebrook, C.F., 1939. Turbulent flow in pipes, with particular reference to the transition region between the smooth and rough pipe laws. J. Inst. Civil Eng., London 11, 133–156.

Colebrook, C.F., White, C.M., 1937. Experiments with fluid friction in roughened pipes. Proc. Royal Soc. London A 161, 367–381.

Cui, J., Patel, V.C., Lin, C.L., 2003. Large-eddy simulation of turbulent flow in a channel with rib roughness. Int. J. Heat Fluid Flow 24, 372–388.

Detert, M., Nikora, V., Jirka, G.H., 2010. Synoptic velocity and pressure fields at the water-sediment interface of streambeds. J. Fluid Mech. 660, 55–86.

Finnigan, J., 2000. Turbulence in plant canopies. Ann. Rev. Fluid Mech. 32, 519–571.

Flack, K.A., Schultz, M.P., 2014. Roughness effects on wall-bounded turbulent flows. Phys. Fluids 26, 1013051.

Han, J.C., Park, J.S., Lei, C.K., 1985. Heat transfer enhancement in channels with turbulence promoters. J. Eng. Gas Turbines Power 107, 628–635.

Hanjalić, K., Launder, B.E., 1972. Fully developed asymmetric flow in a plane channel. J. Fluid Mech. 51, 301–335.

Ho, R.T., Gelhar, L.W., 1973. Turbulent flow with wavy permeable boundaries. J. Fluid Mech. 58, 403–414.

Host-Madsen, A., McCluskey, D., 1994. On the accuracy and reliability of piv measurements, in: 7th Int. Symp. Application of Laser Techniques to Fluid Mechanics, Lisboa, Portugal. pp. 214–226.

Ikeda, T., Durbin, P.A., 2007. Direct simulations of a rough-wall channel flow. J. Fluid Mech. 571, 235–263.

Jarvela, J., 2005. Effect of submerged flexible vegetation on flow structure and resistance. J. Hydraulics 307, 233–241.

Jiménez, J., 2004. Turbulent flows over rough walls. Annu. Rev. Fluid Mech. 36, 173–196.

Jiménez, J., Uhlmann, M., Pinelli, A., Kawahara, G., 2001. Turbulent shear flow over active and passive porous surfaces. J. Fluid Mech. 442, 89–117.

Kong, F.Y., Schetz, J.A., 1982. Turbulent boundary layer over porous surfaces with different surface geometries. Technical Report 82-0030. AIAA.

Kuwata, Y., Suga, K., 2016. Lattice Boltzmann direct numerical simulation of interface turbulence over porous and rough walls. Int. J. Heat Fluid Flow 61, 145–157.

Leonardi, S., Orlandi, P., Djenidi, L., Antonia, R.A., 2004. Structure of turbulent channel flow with square bars on one wall. Int. J. Heat Fluid Flow 25, 384–392.

Leonardi, S., Orlandi, P., Smalley, R.J., Djenidi, L., Antonia, R.A., 2003. Direct numerical simulations of turbulent channel flow with transverse square bars on one wall. J. Fluid Mech. 491, 229–238.

Liu, C.K., Kline, S.J., P., J.J., 1966. An experimental study of turbulent boundary layers on rough walls. Technical Report MD-15.

Lovera, F., Kennedy, J.F., 1969. Friction factors for flat bed flows in sand channels. J. Hydr. Div., ASCE 95, 1227–1234.

Manes, C., Poggi, D., Ridol, L., 2011. Turbulent boundary layers over permeable walls: scaling and near-wall structure. J. Fluid Mech. 687, 141–170.

Manes, C., Pokrajac, D., McEwan, I., Nikora, V., 2009. Turbulence structure of open channel flows over permeable and impermeable beds: A comparative study. Phys. Fluids 21, 125109.

Moody, L.F., 1944. Friction factors for pipe flow. Trans. ASME 66, 671–678.

Nakagawa, H., Tsujimoto, T., Shimizu, Y., 1991. Turbulent flow with small relative submergence, in: Armanini, A., Di Silvio, G. (Eds.), Fluvial Hydraulics of Mountain Regions; Lecture Notes in Earth Sciences 37. Springer Verlag, Berlin, pp. 33–44.

Nepf, H., Ghisalberti, M., 2008. Flow and transport in channels with submerged vegetation. Acta Geophys. 56, 753–777.

Nikora, V., Koll, K., McLean, S., Dittrich, A., Aberle, J., 2002. Zero-plane displacement for rough-bed open-channel flows, in: Int. Conf. Fluvial Hydraulics River Flow 2002, Louvain-la-Neuve, Belgium. pp. 83–92.

Nikuradse, J., 1933. Strömungsgesetze in rauhen rohren. VDI-Forsch. 361.

Nuntadusit, C., Wae-hayee, M., Bunyajitradulya, A., Eiamsa-ard, S., 2012. Thermal visualization on surface with transverse perforated ribs. Int. Commun. Heat Mass Transfer 39, 634 – 639.

Panigrahi, P.K., Schröeder, A., Kompenhans, J., 2008. Turbulent structures and budgets behind permeable ribs. Exp. Therm. Fluid Sci. 32, 1011 – 1033.

Perry, A.E., Schofield, W.H., Joubert, P.N., 1969. Rough wall turbulent boundary layers. J. Fluid Mech. 37, 383–413.

Piomelli, U., 2018. Recent advances in the numerical simulation of rough-wall boundary layers. Phys. Chem. Earth , in press.

Poggi, D., Porporato, A., Ridolfi, L., Albertson, J.D., Katul, G.G., 2004. The effect of vegetation density on canopy sub-layer turbulence. Boundary-Layer Meteorol. 111, 565–587.

Pokrajac, D., Finnigan, J.J., Manes, C., McEwan, I., Nikora, V., 2006. On the definition of the shear velocity in rough bed open channel flows, in: Ferreira, Alves, Leal, Cardoso (Eds.), River Flow 2006. Taylor & Francis, London, pp. 89–98.

Pokrajac, D., Manes, C., 2009. Velocity measurements of a free-surface turbulent flow penetrating a porous medium composed of uniform-size spheres. Transp. Porous, Med. 78, 367–383.

Prasad, A.K., Adrian, R.J., Landreth, C.C., Offutt, P.W., 1992. Effect of resolution on the speed and accuracy of particle image velocimetry interrogation. Exp. Fluids 13, 105–116.

Raupach, M.R., Antonia, R.A., Rajagopalan, S., 1991. Rough-wall turbulent boundary layers. Appl. Mech. Rev. 44, 1–25.

Ruff, J.F., Gelhar, L.W., 1972. Turbulent shear flow in porous boundary. J. Eng. Mech. Div., ASCE 98, 975–991.

Schlichting, H., 1979. Boundary layer theory, 7th edn. McGraw-Hill, New York.

Shimizu, Y., Tsujimoto, T., Nakagawa, H., 1990. Experiment and macroscopic modelling of flow in highly permeable porous medium under free-surface flow. J. Hydrosci. Hydraul. Eng. 8, 69–78.

Suga, K., 2016. Understanding and modelling turbulence over and inside porous media. Flow Turb. Combust. 96, 717–756.

Suga, K., Matsumura, Y., Ashitaka, Y., Tominaga, S., Kaneda, M., 2010. Effects of wall permeability on turbulence. Int. J. Heat Fluid Flow 31, 974–984.

Suga, K., Mori, M., Kaneda, M., 2011. Vortex structure of turbulence over permeable walls. Int. J. Heat Fluid Flow 32, 586–595.

Suga, K., Nakagawa, Y., Kaneda, M., 2017. Spanwise turbulence structure over permeable walls. J. Fluid Mech. 822, 186–201.

Suga, K., Okazaki, Y., Ho, U., Kuwata, Y., 2018. Anisotropic wall permeability effects on turbulent channel flows. J. Fluid Mech. 855. 983–1016.

Suga, K., Tominaga, S., Mori, M., Kaneda, M., 2013. Turbulence characteristics in flows over solid and porous square ribs mounted on porous walls. Flow Turb. Combust. 91, 19–40.

Tani, I., 1987. Turbulent boundary layer development over rough surfaces, in: Meier, H.U., Bradshaw, P. (Eds.), Perspectives in turbulence studies. Springer, Berlin, pp. 233–249.

Wang, L., Salewski, M., Sundén, B., 2010. PIV measurements of turbulent flow in a channel with solid or perforated ribs, in: ASME 2010 3rd Joint US-European Fluids Engineering Summer Meeting: Volume 1, Symposia – Parts A, B, and C, pp. 1995–2003.

Zagni, A.F.E., Smith, K.V.H., 1976. Channel flow over permeable beds of graded spheres. J. Hydraul. Div. 102, 207–222.

Zippe, H.J., Graf, W.H., 1983. Turbulent boundary-layer flow over permeable and non-permeable rough surfaces. J. Hydraul. Res. 21, 51–65.

Table 1: Characteristics of the porous media; $\varphi$, $D_p$, $K$, $C^F$ and $D_p/k$ are porosity, mean pore diameter, permeability, Forchheimer coefficient and the ratio of mean pore diameter to roughness height $k$, respectively.

| Porous Med. | $\varphi$ | $D_p$(mm) | $K$(mm$^2$) | $C^F$(mm) | $D_p/k$ |
|---|---|---|---|---|---|
| #30 | 0.78 | 0.9 | 0.004 | 0.009 | 0.30 |
| #20 | 0.82 | 1.7 | 0.020 | 0.024 | 0.57 |
| #13 | 0.81 | 2.8 | 0.033 | 0.018 | 0.93 |

Table 2: Experimental conditions and measured parameters of solid rib cases; $\mathrm{Re}_b$ and $\mathrm{Re}_\tau$ are the bulk and friction Reynolds numbers; $X_F$ is the separation front; $X_R$ is the reattachment length; the superscript "+" denotes the value normalized by the friction velocity of the bottom rough wall: $u_\tau^R$; $\kappa, d_0, h$ are the von Kármán constant, the zero-plane displacement and the roughness scale; $k_s$ and $\Delta U^+$ are the equivalent sand grain roughness height and the roughness function.

| Case | $\mathrm{Re}_b$ | $\mathrm{Re}_\tau$ | $X_F/k$ | $X_R/k$ | $u_*/U_b$ | $u_\tau^R/U_b$ | $\kappa$ | $d_0^+$ | $d_0/k$ | $h^+$ | $k_s^+$ | $k_s/k$ | $\Delta U^+$ |
|---|---|---|---|---|---|---|---|---|---|---|---|---|---|
| solid | 5000 | 700 | - | 5.1 | 0.16 | 0.18 | 0.41 | 85 | 0.89 | 21 | 685 | 7.1 | 12.5 |
| | 10000 | 1340 | - | 4.9 | 0.16 | 0.17 | 0.40 | 154 | 0.90 | 40 | 1232 | 7.1 | 14.2 |
| | 14900 | 1930 | - | 4.9 | 0.16 | 0.17 | 0.40 | 235 | 0.89 | 56 | 1678 | 6.4 | 15.2 |
| | 20600 | 2600 | - | 5.0 | 0.15 | 0.16 | 0.41 | 328 | 0.90 | 63 | 2023 | 5.6 | 15.3 |
| #30s | 5400 | 680 | - | 4.7 | 0.15 | 0.17 | 0.31 | 100 | 1.09 | 37 | 520 | 5.7 | 16.6 |
| | 11100 | 1320 | - | 4.1 | 0.15 | 0.16 | 0.29 | 183 | 1.10 | 71 | 865 | 5.2 | 19.6 |
| | 14100 | 1670 | - | 4.0 | 0.14 | 0.16 | 0.28 | 230 | 1.10 | 96 | 1067 | 5.1 | 21.2 |
| #20s | 4800 | 570 | - | - | 0.15 | 0.16 | 0.33 | 88 | 1.17 | 32 | 544 | 7.3 | 15.5 |
| | 10400 | 1130 | - | - | 0.13 | 0.14 | 0.29 | 170 | 1.17 | 74 | 839 | 5.8 | 20.2 |
| | 15200 | 1630 | - | - | 0.13 | 0.14 | 0.29 | 242 | 1.19 | 107 | 1214 | 5.9 | 21.5 |
| | 21000 | 2230 | - | - | 0.13 | 0.14 | 0.28 | 338 | 1.18 | 148 | 1569 | 5.5 | 23.1 |
| #13s | 5000 | 580 | - | - | 0.14 | 0.15 | 0.27 | 91 | 1.20 | 38 | 378 | 5.0 | 18.6 |
| | 9900 | 1060 | - | - | 0.13 | 0.14 | 0.24 | 172 | 1.21 | 74 | 588 | 4.2 | 22.7 |
| | 14700 | 1580 | - | - | 0.13 | 0.14 | 0.24 | 251 | 1.25 | 115 | 914 | 4.5 | 24.6 |
| | 20300 | 2230 | - | - | 0.13 | 0.14 | 0.25 | 358 | 1.24 | 150 | 1223 | 4.2 | 25.4 |

Table 3: Experimental conditions and measured parameters of porous rib cases.

| Case | $\mathrm{Re}_b$ | $\mathrm{Re}_\tau$ | $X_F/k$ | $X_R/k$ | $u_*/U_b$ | $u_\tau^R/U_b$ | $\kappa$ | $d_0^+$ | $d_0/k$ | $h^+$ | $k_s^+$ | $k_s/k$ | $\Delta U^+$ |
|---|---|---|---|---|---|---|---|---|---|---|---|---|---|
| #30p | 5000 | 630 | 2.0 | 5.6 | 0.15 | 0.16 | 0.28 | 97 | 1.11 | 41 | 429 | 4.9 | 18.4 |
| | 10500 | 1160 | 2.2 | 5.4 | 0.14 | 0.15 | 0.24 | 184 | 1.14 | 84 | 664 | 4.1 | 23.2 |
| | 15300 | 1630 | 2.3 | 5.5 | 0.13 | 0.14 | 0.23 | 264 | 1.13 | 120 | 866 | 3.7 | 25.7 |
| | 20400 | 2150 | 2.3 | 5.5 | 0.13 | 0.14 | 0.23 | 350 | 1.13 | 160 | 1104 | 3.6 | 27.4 |
| #20p | 5400 | 580 | - | - | 0.14 | 0.15 | 0.24 | 102 | 1.32 | 45 | 341 | 4.4 | 21.1 |
| | 10000 | 1000 | - | - | 0.13 | 0.14 | 0.23 | 177 | 1.34 | 78 | 538 | 4.1 | 24.3 |
| | 14900 | 1450 | - | - | 0.12 | 0.13 | 0.22 | 252 | 1.31 | 110 | 727 | 3.8 | 26.3 |
| | 19900 | 1890 | - | - | 0.12 | 0.13 | 0.22 | 333 | 1.32 | 140 | 926 | 3.7 | 27.3 |
| #13p | 4900 | 510 | - | - | 0.13 | 0.14 | 0.24 | 107 | 1.39 | 37 | 290 | 3.8 | 19.8 |
| | 10100 | 950 | - | - | 0.12 | 0.13 | 0.22 | 183 | 1.37 | 72 | 466 | 3.5 | 24.6 |
| | 14900 | 1410 | - | - | 0.12 | 0.13 | 0.22 | 279 | 1.40 | 110 | 698 | 3.5 | 26.7 |
| | 19900 | 1900 | - | - | 0.12 | 0.13 | 0.22 | 381 | 1.46 | 145 | 959 | 3.7 | 27.5 |

Table 4: Roughness parameters for solid impermeable case by the classical method; $\Delta U^+$, $k_s^{N+}$ and $u_\tau^N$ are obtained by Eqs. (1) and (3).

| Case | $\mathrm{Re}_b$ | $\Delta U^+$ | $k_s^{N+}$ | $u_*^N/u_*$ |
|---|---|---|---|---|
| solid | 5000 | 12.7 | 880 | 1.10 |
| | 10000 | 14.9 | 1540 | 1.07 |
| | 14900 | 15.1 | 2180 | 1.08 |
| | 20600 | 14.9 | 2970 | 1.02 |

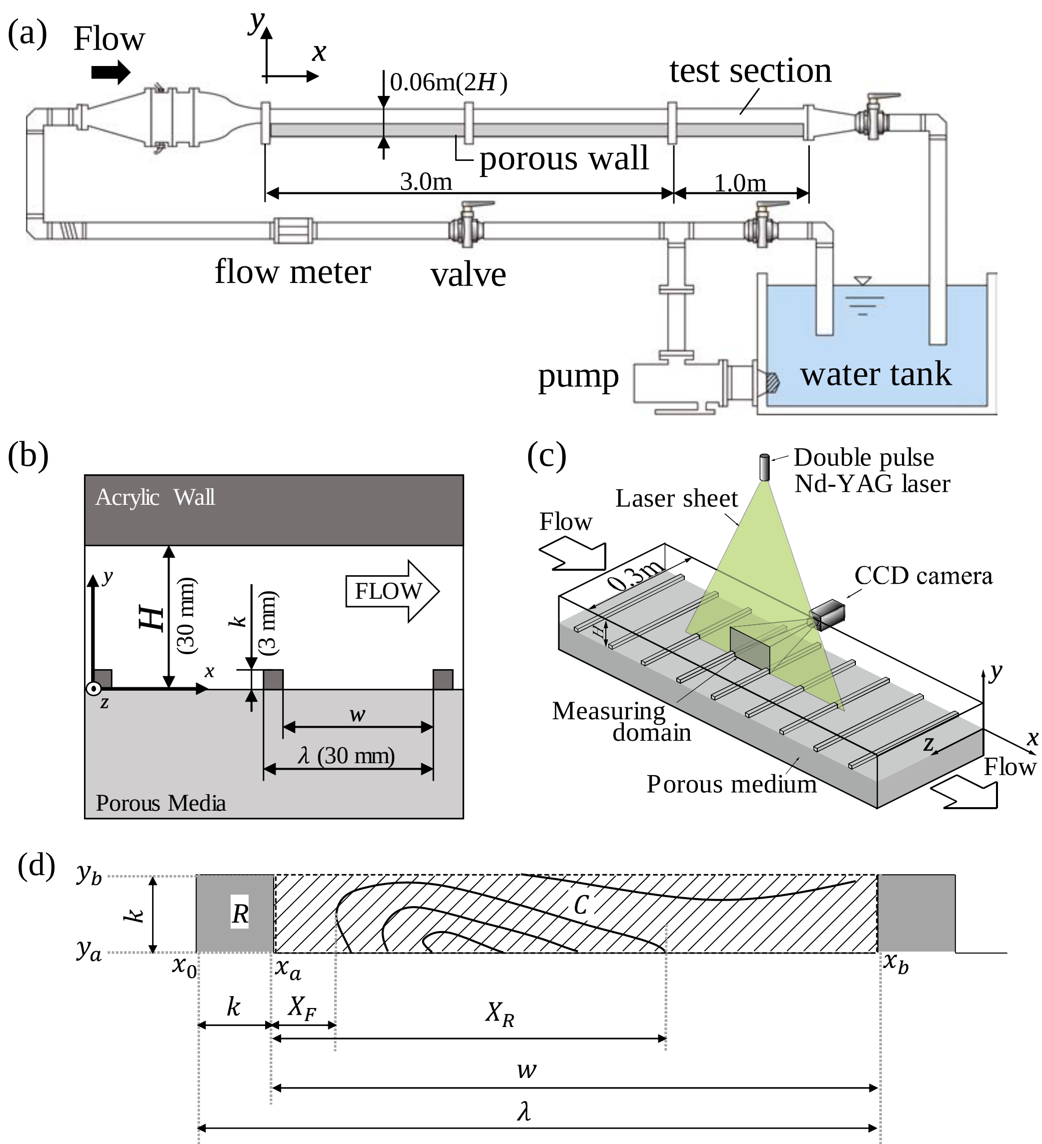


Figure 1: Experimental set-up: (a) schematic view of the flow facility, (b) cross-sectional view of the test section, (c) schematic view of the test section, (d) schematic view of the rib roughness and definitions of geometrical parameters: $X_F$ and $X_R$ correspond to the location of $\bar{u} = 0$ nearest upstream and downstream rib, respectively.

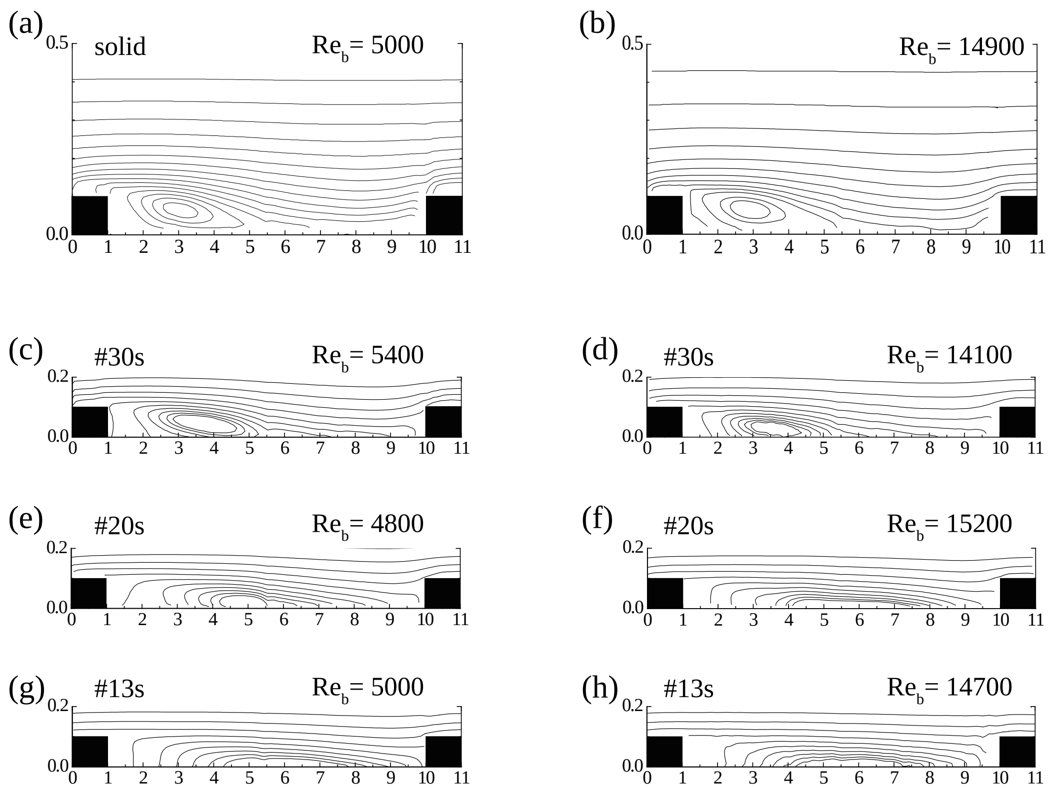


Figure 2: Streamlines of solid-rib roughened cases: (a, b) case solid at $\mathrm{Re}_b \simeq 5000, 14900$, (c, d) case #30s at $\mathrm{Re}_b = 5400, 14100$, (e, f) case #20s at $\mathrm{Re}_b = 4800, 15200$, (g, h) case #13s at $\mathrm{Re}_b = 5000, 14700$.

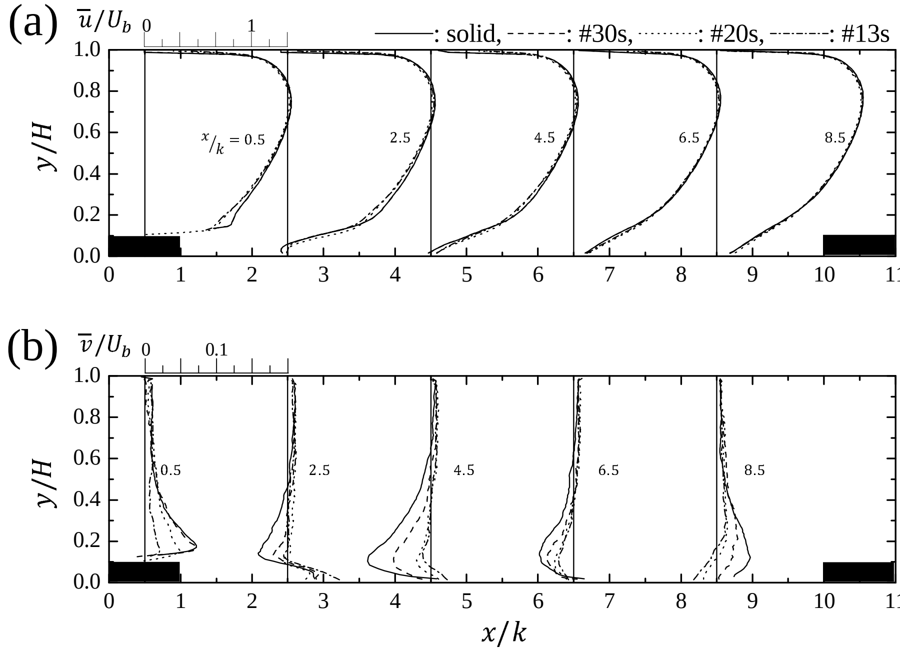


Figure 3: Profiles of mean velocity of cases solid, #30s, #20s and #13s at $\mathrm{Re}_b \simeq 15000$: (a) streamwise mean velocity, (b) wall-normal mean velocity.

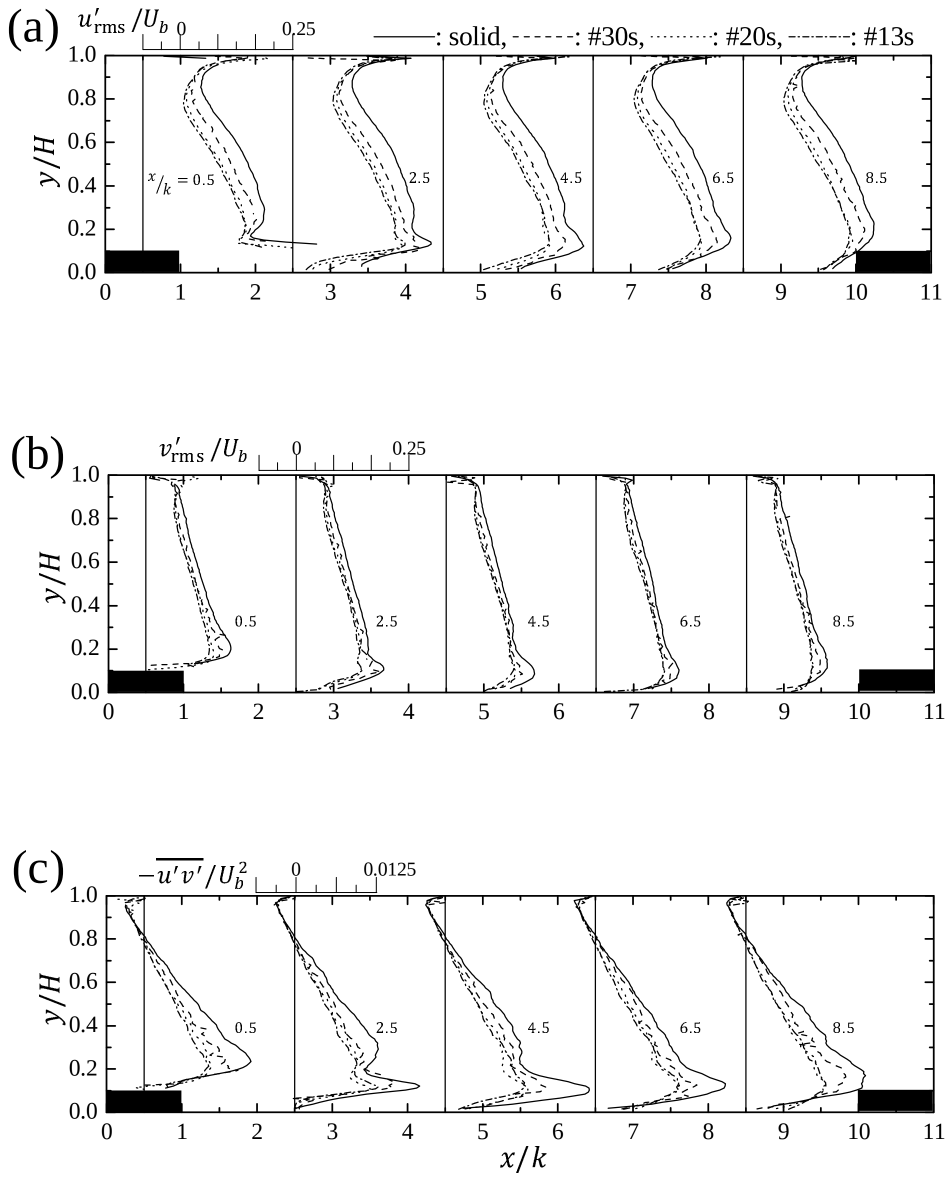


Figure 4: Profiles of mean turbulence statistics of cases solid, #30s, #20s and #13s at $\mathrm{Re}_b \simeq 15000$: (a) streamwise rms velocity, (b) wall-normal rms velocity, (c) Reynolds shear stress.

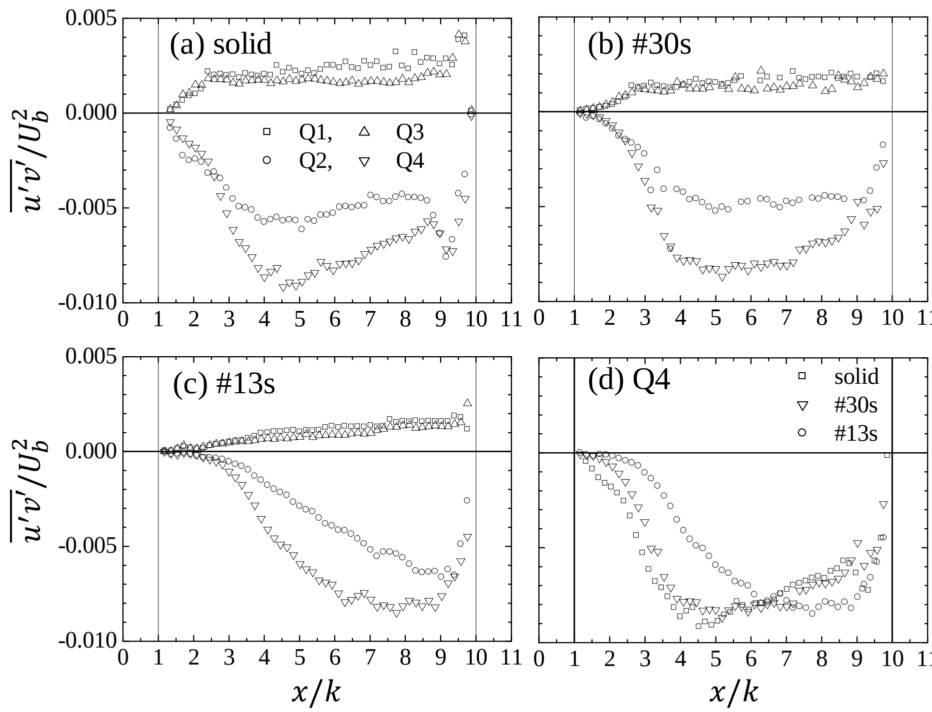


Figure 5: Decomposed Reynolds shear stress at $y/k \simeq 0.33$, $\mathrm{Re}_b \simeq 15000$: (a) case solid, (b) case #30s, (c) case #13s, (d) comparison of Q4.

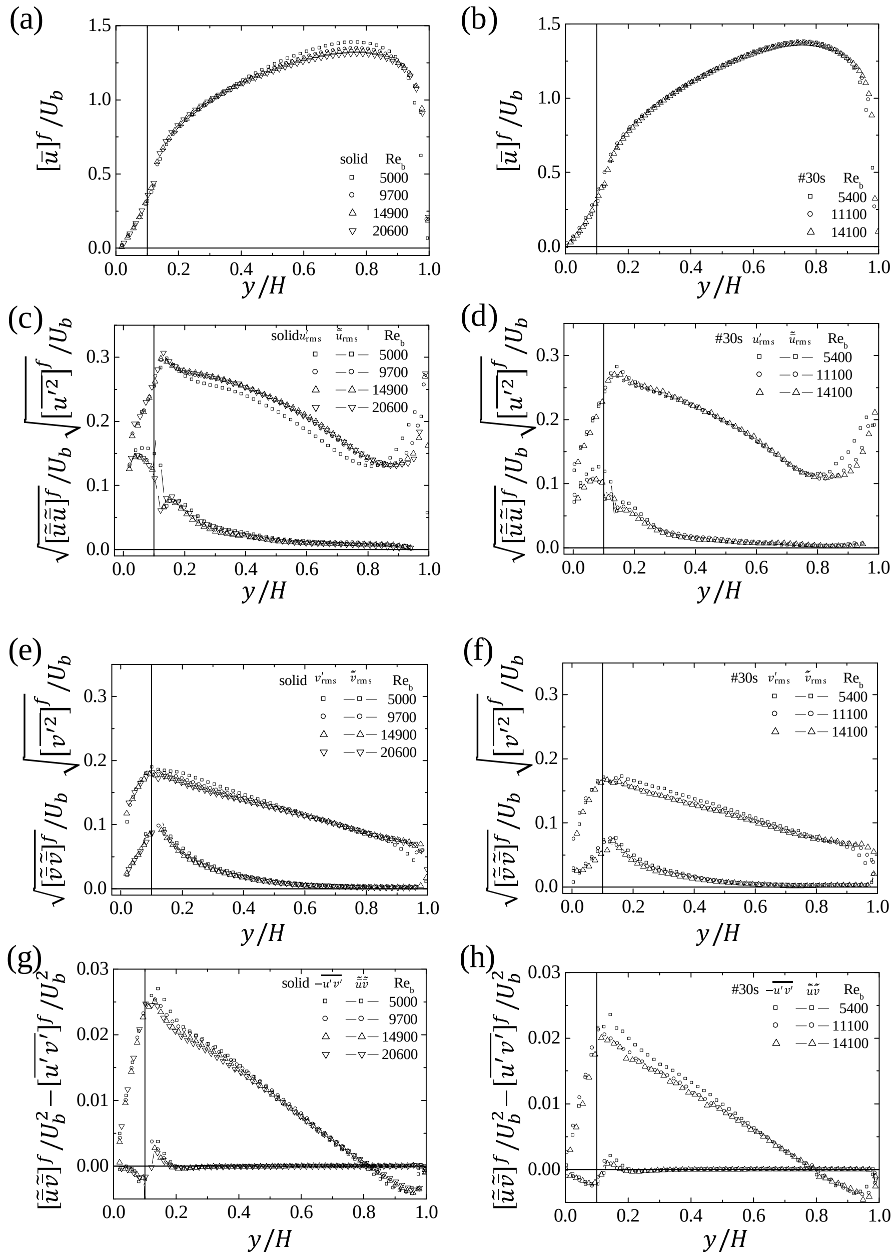

Figure 6: Plane averaged mean turbulence statistics of cases solid at $\mathrm{Re}_b = 5000 - 20600$ and #30s at $\mathrm{Re}_b = 5000 - 14100$: (a, b) mean velocity, (c, d) streamwise rms velocity and velocity dispersion, (e, f) wall-normal rms velocity and velocity dispersion, (g, h) Reynolds shear stress and dispersion shear stress.

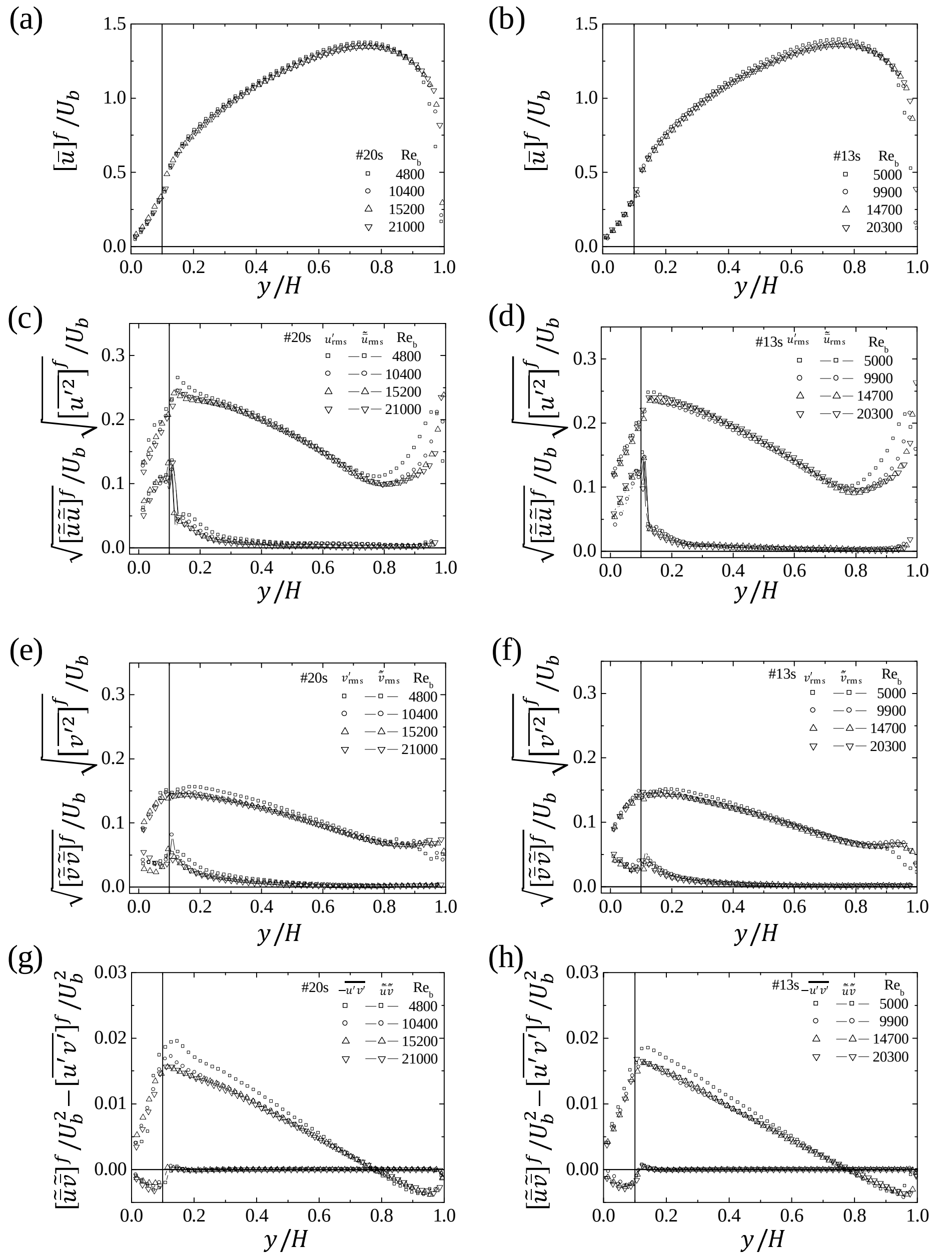

Figure 7: Plane averaged mean turbulence statistics of cases #20s at $\mathrm{Re}_b \simeq 4800-21000$ and #13s at $\mathrm{Re}_b = 5000-20300$: (a, b) mean velocity, (c, d) streamwise rms velocity and velocity dispersion, (e, f) wall-normal rms velocity and velocity dispersion, (g, h) Reynolds shear stress and dispersion shear stress.

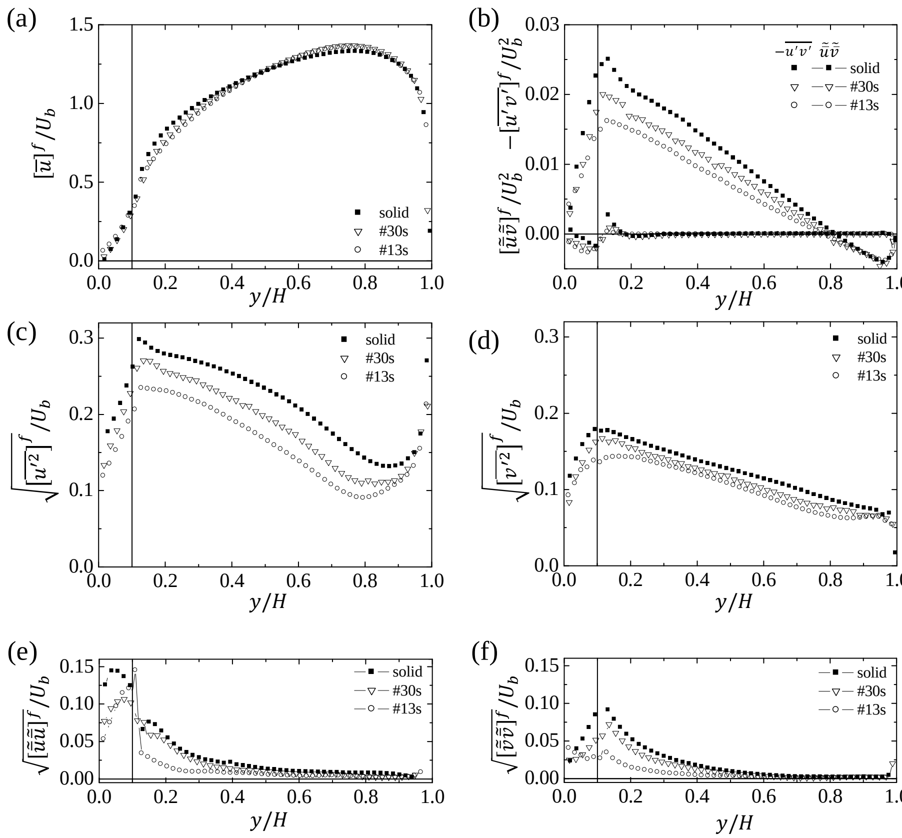

Figure 8: Plane averaged mean turbulence statistics of cases solid, #30s and #13s at $\mathrm{Re}_b \simeq 15000$: (a) mean velocity, (b) Reynolds shear stress and dispersion stress, (c) streamwise rms velocity, (d) wall-normal rms velocity, (e) streamwise velocity dispersion, (f) wall-normal velocity dispersion.

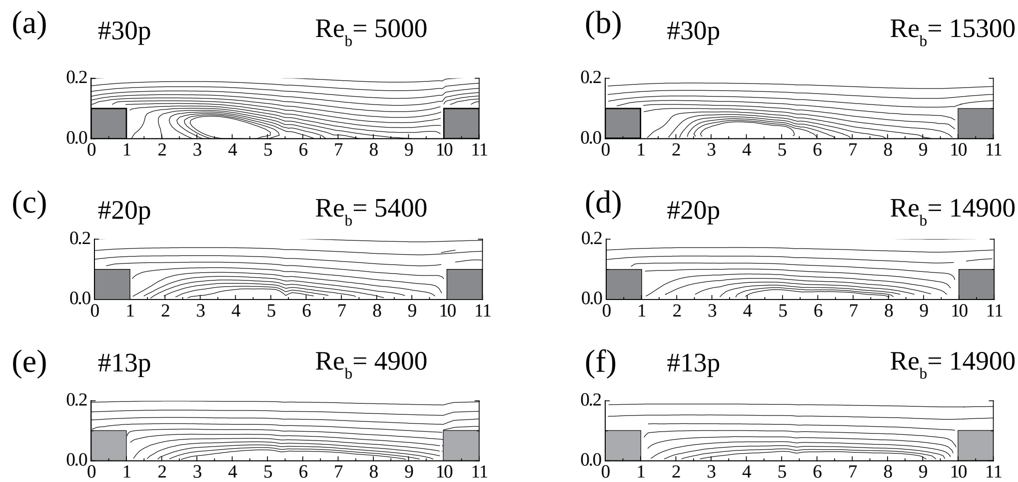


Figure 9: Streamlines of porous-rib roughened cases: (a, b) case #30p at $\mathrm{Re}_b = 5000, 15300$, (c, d) case #20p at $\mathrm{Re}_b = 5400, 14900$, (e, f) case #13p at $\mathrm{Re}_b = 4900, 14900$ .

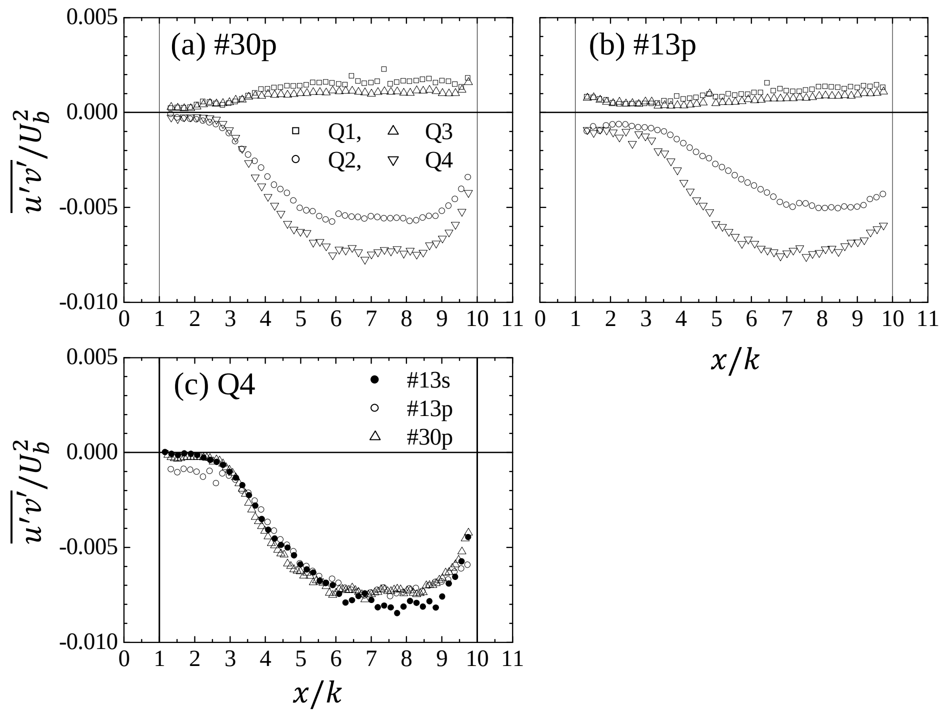


Figure 10: Decomposed Reynolds shear stress at $y/k \simeq 0.33$, $\mathrm{Re}_b \simeq 15000$: (a) case #30p, (b) case #13p, (c) comparison of Q4 of cases #13s, #13p and #30p.

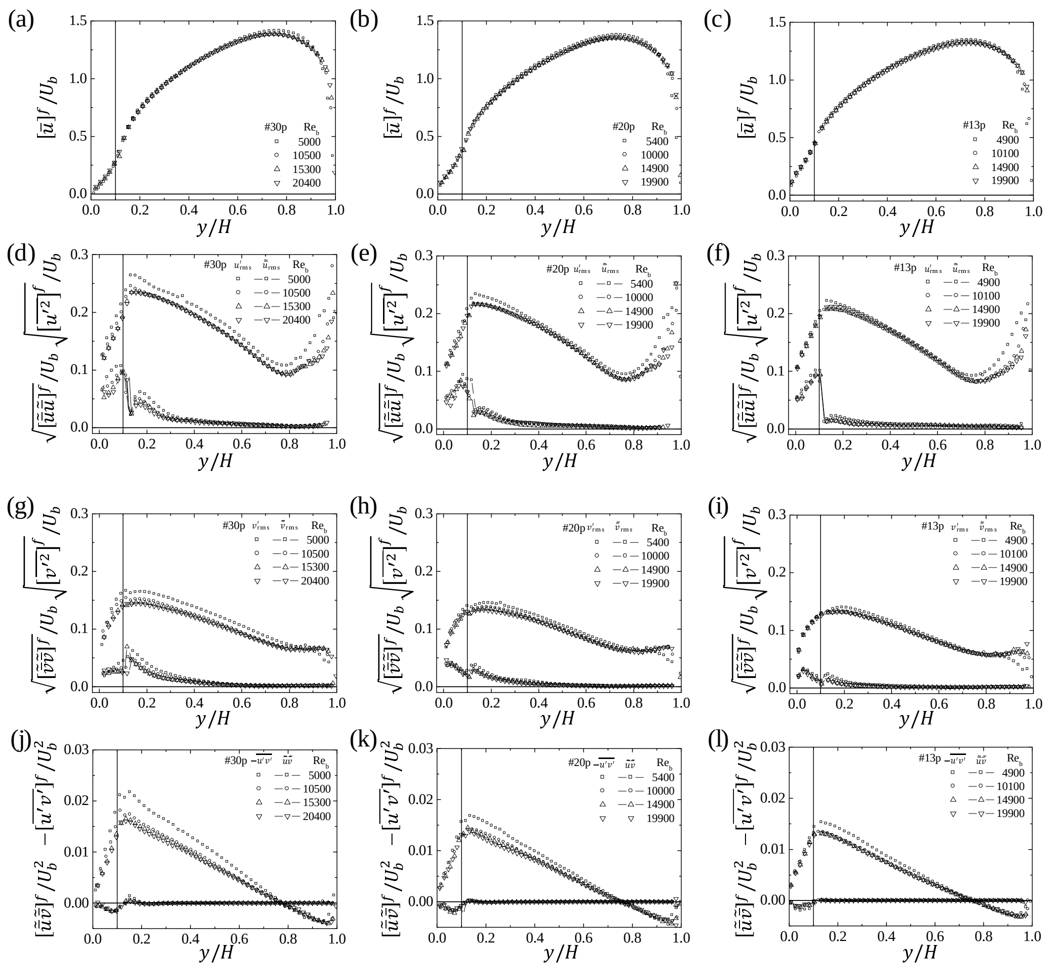


Figure 11: Plane averaged mean turbulence statistics of cases #30p at $\mathrm{Re}_b = 5000-20400$, #20p at $\mathrm{Re}_b = 5400 - 19900$ and #13p at $\mathrm{Re}_b = 4900 - 19900$: (a, b, c) mean velocity, (d, e, f) streamwise rms velocity and velocity dispersion, (g, h, i) wall-normal rms velocity and velocity dispersion, (j, k, l) Reynolds shear stress and dispersion shear stress.

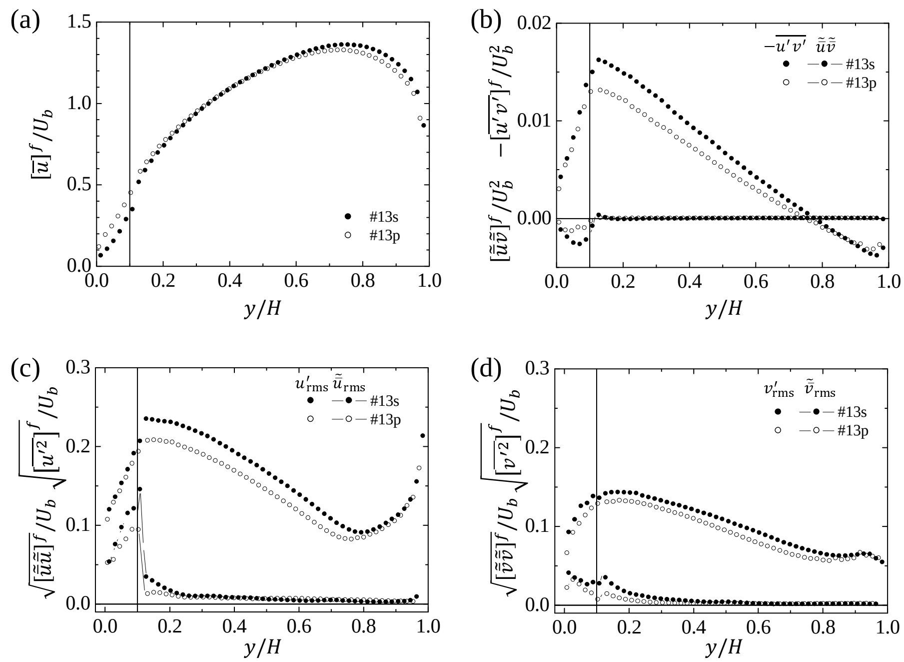


Figure 12: Plane averaged mean turbulent statistics of cases #13p and #13s at $\mathrm{Re}_b \simeq 15000$: (a) mean velocity, (b) Reynolds and dispersion shear stresses, (c) streamwise rms velocity and velocity dispersion, (d) wall-normal rms velocity and velocity dispersion.

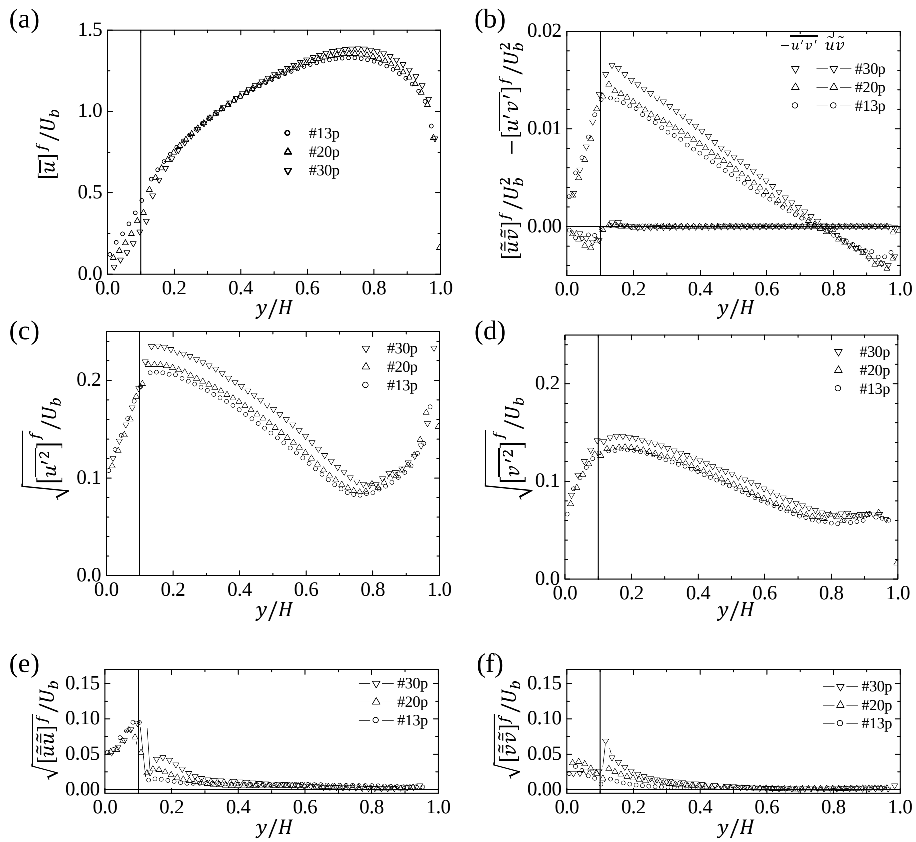

Figure 13: Plane averaged mean turbulent statistics of cases#30p, #20p and #13p at $\mathrm{Re}_b \simeq 15000$: (a) mean velocity, (b) Reynolds and dispersion shear stresses, (c) streamwise rms velocity, (d) wall-normal rms velocity, (e) streamwise velocity dispersion, (f) wall-normal velocity dispersion.

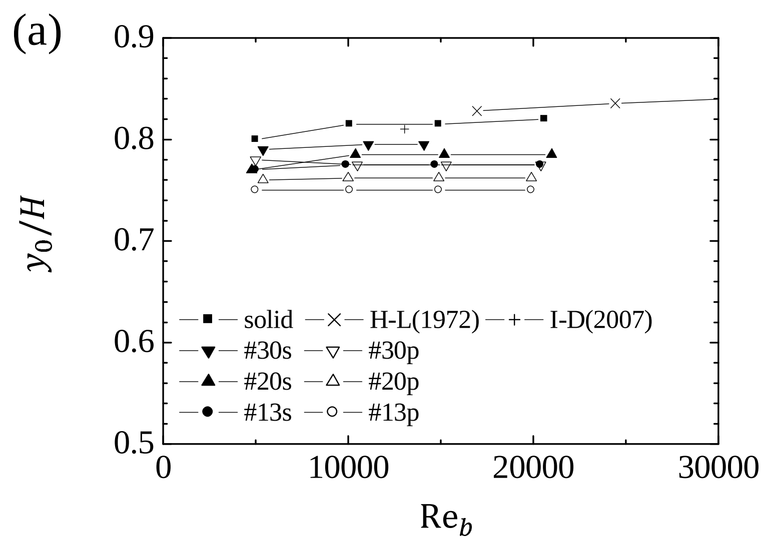


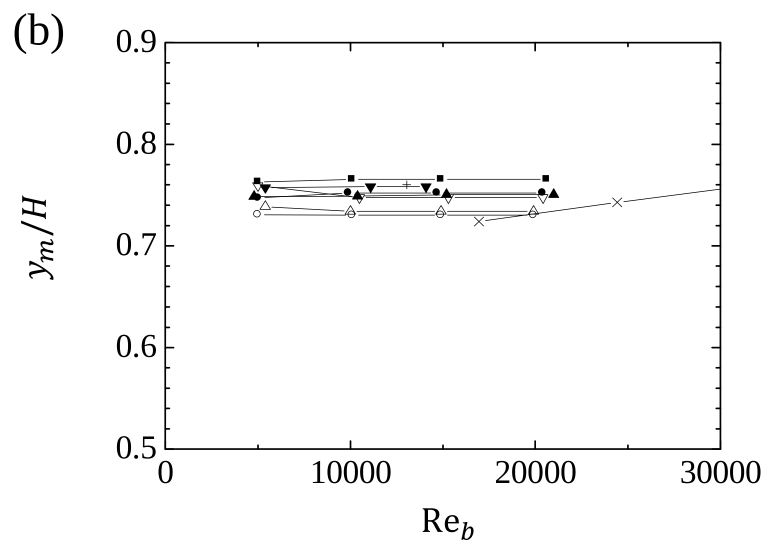


Figure 14: Variation of the zero-shear stress point and the maximum mean velocity location: (a) zero-shear stress point $y_0$, (b) maximum mean velocity location $y_m$. H-L and I-D corresponds to Hanjalić and Launder (1972) and Ikeda and Durbin (2007), respectively.

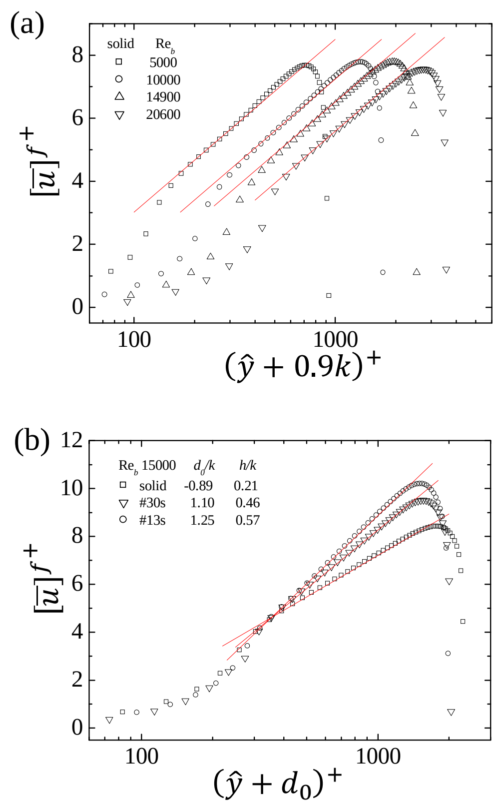


Figure 15: Mean velocity distribution in semi-logarithmic chart: (a) case solid fitted to Eq.(1), (b) comparison of the profiles fitted to Eq.(4) for cases solid #30s and #13s. Red lines are fitting lines.

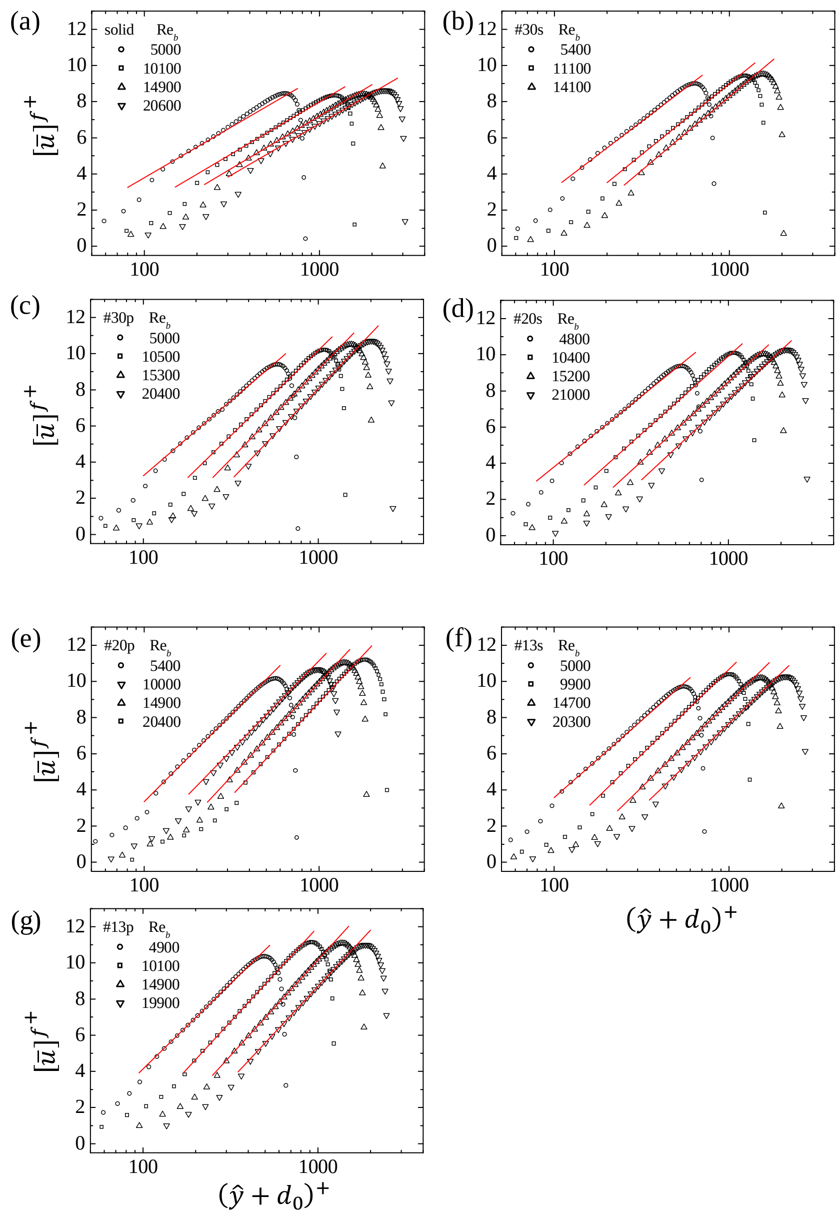


Figure 16: Mean velocity distributions in semi-logarithmic chart: (a) case solid, (b) case #30s, (c) case #30p, (d) case #20s, (e) case #20p, (f) case #13s, (g) case #13p. Red lines are fitting lines of Eq.(4).

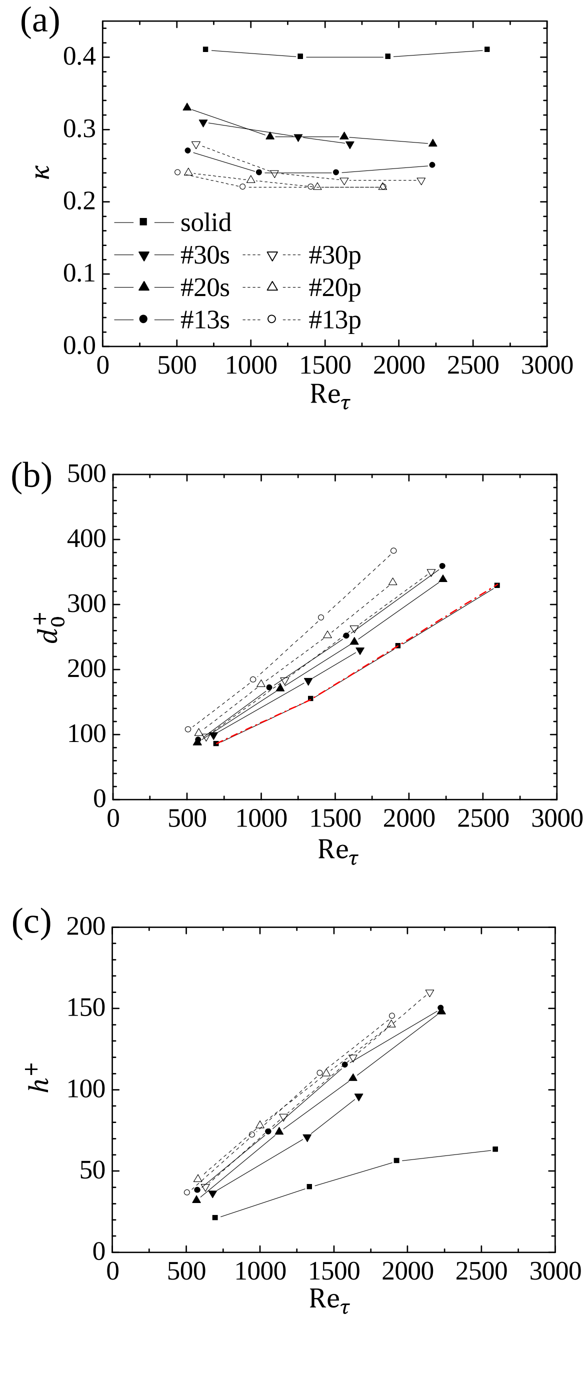


Figure 17: Distributions of log-law parameters against the friction Reynolds number $\mathrm{Re}_\tau$;: (a) von Kármán constant, (b) zero-plane displacement, (c) roughness scale. In (b) the red chain line corresponds to the mean roughness height: $0.9k$.

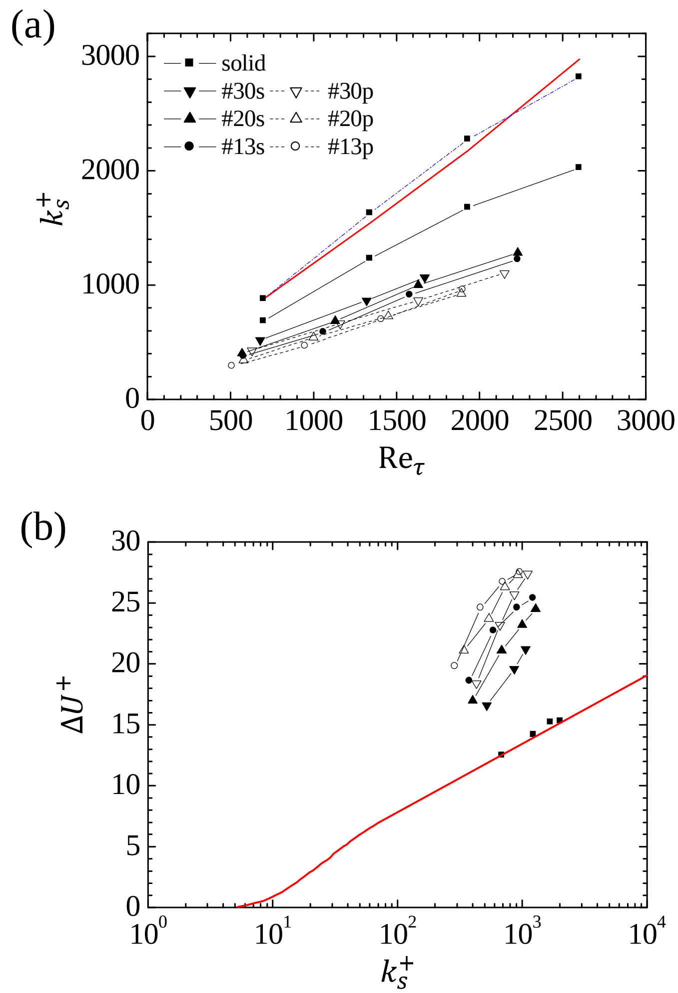


Figure 18: Distributions of roughness parameters: (a) equivalent sand grain roughness $k_s^+$, (b) roughness function $\Delta U^+$. The blue chain line in (a) corresponds to the values for case solid obtained with the bed shear stress. Red lines in (a) and (b) correspond to the profiles of $k_s^{N+}$ and $\Delta U^+$ for uniform sand roughness by Schlichting (1979), respectively.

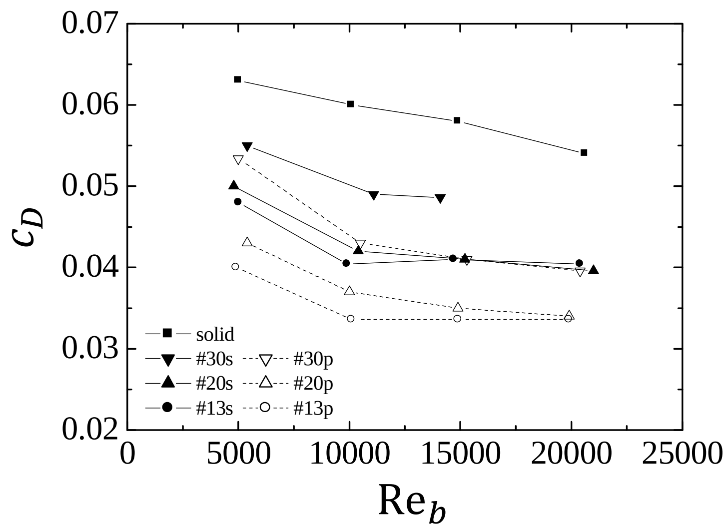


Figure 19: Variation of drag coefficient against the bulk Reynolds number.